Pile-template interaction during offshore pile driving

J.A.G. de Ruiter

Technical University of Delft

Pile-template interaction during offshore pile driving

by

J.A.G. de Ruiter

in partial fulfillment to obtain the degree of Master of Science
at the Delft University of Technology,
to be defended publicly on Friday June 23, 2023 at 13:00.

Student number:	4375173	
Project duration:	September 1, 2021 – June 23, 2023	
Thesis committee:	Prof. dr. A. V. Metrikine,	TU Delft - Chairman
	ir. J. S. Hoving,	TU Delft - Supervisor
	ir. M. M. Stofregen,	Huisman Equipment B.V. - Supervisor

This thesis is confidential and cannot be made public until June 23, 2025.

Preface

This report presents my thesis on analyzing the pile-structure interaction using a pre-piling template during pile driving. Work that has been conducted to complete the requirements for the degree of Master of Science in Offshore and Dredging Engineering. It represents the last chapter of my studies at the Delft University of Technology which I started with a Bachelor of Science in Marine Technology.

This thesis was performed in cooperation with Huisman. Working with the individuals at Huisman has been an absolute pleasure, and I have thoroughly enjoyed the stimulating atmosphere they provide. I want to thank Matthijs Stofregen for his daily supervision at Huisman and critical feedback on my project process. Thank you, Jeroen Hoving, for the supervision and meetings at the TU Delft, which was very helpful in understanding the problem and overcoming problems during the model's development. Alongside my supervisors, I would like to thank my TU chairman, Andrei Metrikine, for his time and valuable input on the research.

Finally, I would like to thank my family and friends who have supported and helped me throughout my time in Delft, especially during this last part. With all of you, those years have been fantastic.

J.(Jop) A.G. de Ruiter
Rotterdam, June 2023

Abstract

In recent years the global energy demand has rapidly increased and will continue to grow in the next decades. With the growing demand for energy and the international agreement to use more renewable energy, the offshore wind industry is developing rapidly. This causes offshore wind farms to be installed at locations with larger water depths and wind turbines becoming larger and heavier, leading to the use of support jackets. Due to this trend, pre-piling templates are used more often in the industry to decrease the installation time and increase the accuracy of offshore wind parks supported by jackets. Pre-piling templates are made to align and guide foundation piles during pile driving. Huisman built a pre-piling template to install two offshore wind farms off the coast of Taiwan. After installation, it turned out that the secondary steel on the template was severely damaged. In this thesis, research is done to identify the possible reasons for damage to the secondary steel of the pre-piling template during pile driving.

An investigation of currently available literature has identified possible causes of increasing loads on pre-piling templates. The difference between most of the pre-piling templates investigated in the literature and the template of Huisman is the use of friction pads instead of rollers to guide and align the foundation piles during installation. In addition to aligning and guiding the foundation piles, friction pads also clamp the pile. Based on a thorough literature review and the current design of the template, a hypothesis regarding the cause of the damage was formulated. The hypothesis states that the current design of the template causes an increase in normal force and friction force between the pile and the pads during pile driving, damaging the secondary steel of the pre-piling template.

To test the hypothesis, a model is developed to describe and analyze the dynamic interaction between the template and foundation pile during pile driving. The model exists of an external hammer force, a LuGre dynamic friction element to represent soil-pile interaction and a part representing the stick-slip interaction between the pile and the pre-piling template. The model has been implemented using Matlab to generate the system response in the time domain from the corresponding equations of motion. The different components of the model are validated and verified using field data and data from the literature. While the model has been fully verified, the model could not be quantitatively validated due to a lack of data. Still, the model has been qualitatively validated based on trends from the literature.

The use of friction pads leads to energy transfer from the hammer blows into the template due to the existing friction forces between the pile and the pads. Additionally, results show an increase in normal force between the friction pads and the pile during a hammer blow due to the design of the centralizer. The rotation of the upper centralizer causes an increase in normal force between the pile and pad due to its orientation. The increasing normal force causes an increase in friction force between the pile and the template, which influences the stick-slip behavior between the pile and the pad. A higher friction force leads to less pile penetration and therefore increases the number of blows required to reach penetration depth, thereby increasing the template's exposure to the hammer blows during pile installation. The energy dissipation into the template and the increased load cycles due to the use of pads and the current design of the template could cause damage to the secondary steel of the template. It is recommended to incorporate the secondary steel and the template in the model to perform a more detailed analysis of vibrations and local stresses in the template and secondary steel. Also, add flexibility to the pile to allow for radial expansion and wave propagation due to pile driving. Finally, it is recommended to consider hydrodynamic loads to analyze the effect on the installation process and the possible changes to the energy flow. Foundation piles can sway and bend due to these loads.

Contents

List of Figures

Nomenclature

Symbol	Definition	Unit
c	Speed of sound in steel	$[m/s]$
c_{cyl}	Damping of the hydraulic cylinder	$[Ns/m]$
c_{soilp}	Plastic soil damping	$[Ns/m]$
e	Euler's number	$[-]$
E_{hammer}	Hammer energy	$[J]$
$F(t)$	Hammer force	$[N]$
$\bar{F}(t)$	Dimensionless hammer force	$[N]$
F_c	Kinetic friction force	$[N]$
F_{crit}	Critical friction force	$[N]$
F_h	Horizontal force between pile and pad	$[N]$
F_{pre}	Pretension force	$[N]$
F_s	Static friction force	$[N]$
F_{soil}	Soil force	$[N]$
F_v	Vertical force between pile and pad	$[N]$
g	Gravitational acceleration	$[m/s^2]$
$I_{triangle}$	Mass moment of inertia of the upper centralizer	$[kgm^2]$
k_c	Cushion stiffness	$[N/m]$
$\bar{k}_c$	Dimensionless cushion stiffness	$[N/m]$
k_{cyl}	Stiffness of the hydraulic cylinder	$[N/m]$
k_{eq}	Equivalent radial stiffness of the pile	$[N/m]$
L_α	Perpendicular length between point C and hydraulic cylinder	$[m]$
L_β	Length of the upper centralizer between point A and C	$[m]$
L_2	Length of the upper centralizer between point B and C	$[m]$
m_{pad}	Mass of the friction pad	$[kg]$
m_{pile}	Mass of the pile	$[kg]$
m_r	Mass of the ram	$[kg]$
M_{cyl}	Moment around point C due to the hydraulic cylinder	$[Nm]$
M_h	Moment around point C due to F_h	$[Nm]$
M_{pad}	Moment around point C due to the mass of the pad	$[Nm]$
M_{pre}	Moment around point C due to the pretension	$[Nm]$
M_v	Moment around point C due to F_v	$[Nm]$
P	Power	$[watts]$
t	time	$[s]$
u_a	Displacement of the anvil in vertical direction	$[m]$
$\dot{u}_a$	Velocity of the anvil in vertical direction	$[m/s]$
u_r	Displacement of the ram in vertical direction	$[m]$
$\ddot{u}_r$	Acceleration of the ram	$[m/s^2]$
U_d	Initial displacement of point D	$[m]$
v_{rel}	Relative velocity between the pile and pad	$[m/s]$
v_0	Impact velocity of the ram	$[m]$
W	Work	$[J]$
z_{LuGre}	Internal displacement of the LuGre element in vertical direction	$[m]$

Symbol	Definition	Unit
$\dot{z}_{LuGre}$	Internal velocity of the LuGre element in vertical direction	$[m]$
z_{pad}	Displacement of the pad in vertical direction	$[m]$
$\dot{z}_{pad}$	Velocity of the pad in vertical direction	$[m/s]$
$\ddot{z}_{pad}$	Acceleration of the pad in vertical direction	$[m/s^2]$
z_{pile}	Displacement of the pile in vertical direction	$[m]$
$\dot{z}_{pile}$	Velocity of the pile in vertical direction	$[m/s]$
$\ddot{z}_{pile}$	Acceleration of the pile in vertical direction	$[m/s^2]$
α	Angle between L_2 and L_α	$[rad]$
β	Angle between L_β and horizontal axis	$[rad]$
θ	Rotational displacement of the upper centralizer	$[rad]$
$\dot{\theta}$	Rotational velocity of the upper centralizer	$[rad/s]$
$\ddot{\theta}$	Rotational acceleration of the upper centralizer	$[rad/s^2]$
ϑ	Stribeck velocity	$[m/s]$
μ_d	Dynamic friction coefficient	$[-]$
μ_s	Static friction coefficient	$[-]$
σ_0	Soil stiffness	$[N/m]$
σ_1	Soil damping	$[Ns/m]$
σ_2	Dynamic friction coefficient	$[-]$

1

Introduction

1.1. Huisman

Huisman provides sustainable and innovative solutions for the world's leading companies in heavy lifting, oil and gas, offshore renewable energy, naval and leisure markets. Its headquarter is located in Schiedam, The Netherlands. In Figure 1.1, a picture of the Huisman yard, factory and offices can be seen. Since its founding in 1929, Huisman has established a solid reputation for providing clients worldwide with high-quality products and services. Huisman's product line includes offshore wind tools, pipe-lay equipment, cranes, winches, drilling systems, and other heavy-duty machinery that meet the exacting demands of the offshore and onshore industries. The company's expertise varies from concept to installation and lifetime support. It also identifies technical solutions, ranging from highly engineered integrated systems to stand-alone components [1]. This thesis research is performed under co-supervision and using the facilities of Huisman.

Figure 1.1: The Huisman yard, factory and offices in Schiedam

1.2. Problem description

1.2.1. The offshore wind industry

The global energy demand has rapidly increased in recent years, driven by population growth, economic development, and technological advancements [2]. This trend is projected to continue in the coming decades, with the US Energy Information Administration predicting that world energy consumption will grow by almost 50% between 2018 and 2050 [3]. Nowadays, the main production of energy comes from fossil fuels, which contribute to climate change due to greenhouse gas emissions resulting from these fossil fuels. In response, the international community has set targets for reducing carbon emissions and transitioning to renewable energy sources, as outlined in the Paris Agreement [4]. To be able to reach these targets, the main source of energy needs to be shifted from fossil fuels to renewable energy. Solar, wind, hydro, tidal, geothermal and biomass energy are the most common renewable energy sources offering a cleaner and more sustainable alternative to fossil fuel. According to the

International Renewable Energy Agency, the wind energy industry is one of the fastest-growing sectors in the renewable energy industry. In 2021 a worldwide installed wind power capacity of 823 GW has been reached [5].

The total offshore wind power capacity was 54 GW in 2021, which is 6.5% of the total wind power capacity. However, since 2018 the total offshore capacity has doubled and the onshore capacity has increased by 42%. The offshore wind energy sector is growing rapidly due to higher and more constant wind speeds and the availability of potential sites. Another reason offshore wind grows faster is because onshore wind turbines are visually and noise-polluting in inhabited areas.

The first offshore wind farm was produced in Denmark in 1991. This wind farm has a capacity of 5 MW consisting of eleven turbines and is called Vindeby [6]. The real potential of the offshore wind industry to provide large-scale wind energy was demonstrated in the early 2000s by building several large-scale wind farms among which Middelgrunden off the coast of Copenhagen was the first in 2000 with a total capacity of 80 MW [7]. Nowadays, the total capacity is 54 GW. Wind turbines have developed from 2 MW turbines in the early 2000s to 13 MW turbines in 2021. In a few years, wind turbines with a capacity of 20 MW are expected. This enormous increase in capacity and dimensions yields many new challenges for installing these turbines.

1.2.2. Offshore wind support structures

Installing wind turbines offshore gives some challenges compared to onshore wind turbines. First, offshore wind turbines are subject to hydrodynamic and aerodynamic loads. Also, the type of foundation does matter a lot offshore. Onshore usually, concrete foundations are used, while offshore the type of foundation mainly depends on the water depth. In this section, the most used types of offshore foundations are explained.

The variety of support structures can be split up into two groups. The first group of structures are bottom-founded structures and the second group are floating offshore structures. The bottom-founded group exists of gravity-based, monopile, caisson, tripod and jacket structures (see Figure 1.2). The floating support structures consist of spar buoys, tension leg platforms and barges. Floating offshore structures are suitable in water depths deeper than 100m. The water depth used in this thesis is shallower than 100m, so only bottom-founded structures are relevant for this research [8].

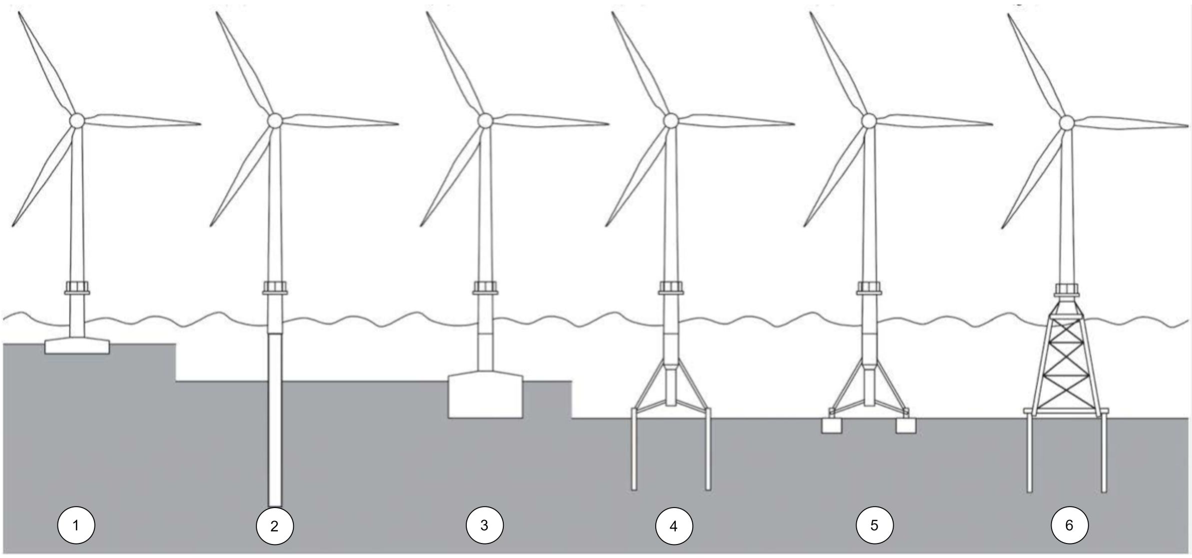

Figure 1.2: Bottom-founded wind support structures, from left to right 1. gravity-based 2. monopile 3. caisson 4. tripod with foundation piles 5. tripod with suction anchors 6. jacket [9]

The choice between the different types of bottom-founded support structures depends on multiple criteria, such as water depth, environmental conditions and financial limits. Water depth often has the largest impact on the choice of the foundation. Typically, gravity-based foundations are used in waters with a depth of up to 27m. Monopiles usually are installed up to 40m water depth. Tripods are more suitable for water-depth up to 80 meters. For a depth between 40 and 100m, jackets are commonly used. In 2020, the percentages of bottom-founded support structures for offshore wind turbines in Europe based on accumulative data can be seen in Figure 1.3. Since the start of the offshore wind industry, monopiles have been the most favorable due to the ease of fabrication and installation with 82.7% [8]. As the water-depth increase, the use of jackets is more viable.

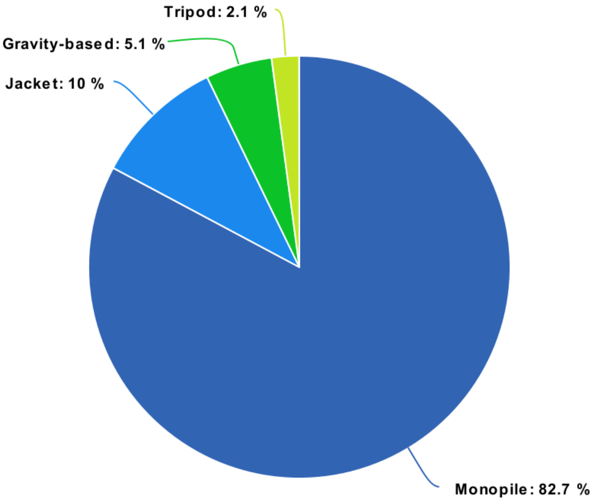

Figure 1.3: Distribution of bottom-founded offshore wind support structures until 2020 in Europe [10]

1.3. Problem definition

An example of two projects where a jacket is chosen as a support structure is the two offshore wind turbine parks located off the coast of Taiwan, called Changfang and Xidao. These wind parks have a combined capacity of 589 MW consisting of 62 wind turbines that each have a capacity of 9.5 MW [11]. Three-legged jackets support these wind turbines, which are held in place by three foundation piles, each located at one leg. A typical example of a three-legged jacket can be seen in Figure 1.4a. In Figure 1.4b, different parts of the jacket can be seen.

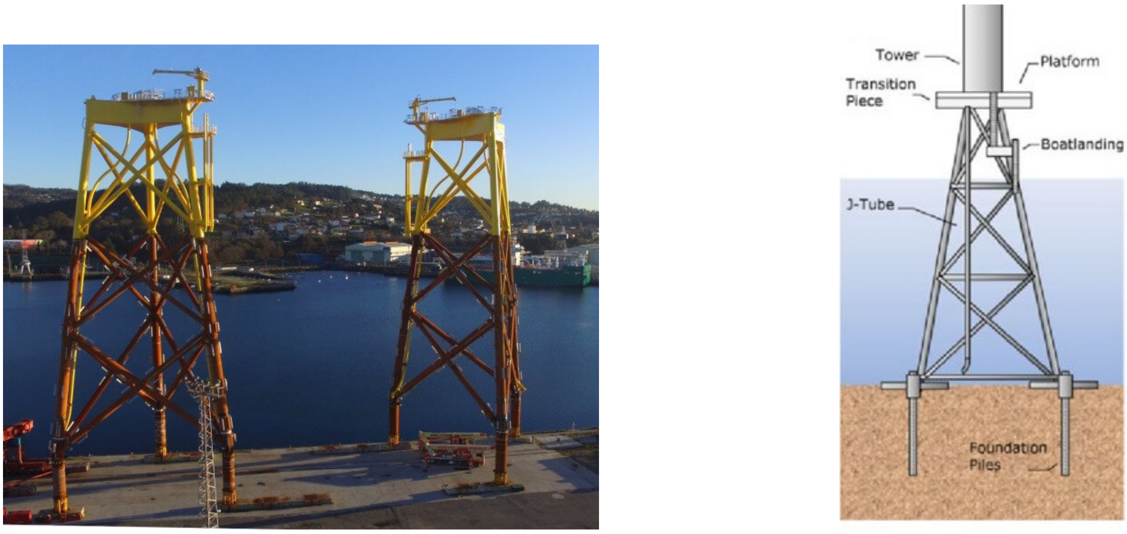

(a) A typical example of an offshore wind turbine support jacket with three legs [12]

(b) Schematic front view of a jacket with foundation piles [13]

Figure 1.4: An example and schematic overview of an offshore jacket support structure

There are two ways to install a jacket foundation, pre-piling and post-piling. First, the foundation piles must be installed to install a jacket with the pre-piling method. After the installation of the foundation piles, the jacket will be lowered to the seabed and attached to the foundation piles. A typical jacket installed using the pre-piling method can be seen in Figure 1.4a. The pre-piling method is often used in offshore wind projects with many jackets, such as Changfang and Xidao, it could be beneficial to develop and use a pre-piling template. Huisman built one for Changfang and Xidao.

To install a jacket foundation with the post-piling method, first, the jacket is placed on the seabed, after which the foundation piles are installed through the legs or the sleeves around the legs of the jacket, see Figure 1.5. In Figure 1.5, a jacket can be seen where the foundation piles are installed through the legs and a jacket can be seen where the foundation piles are installed in the sleeves around the legs. Post-piling often happens in one-off offshore projects, such as installing a large offshore oil platform.

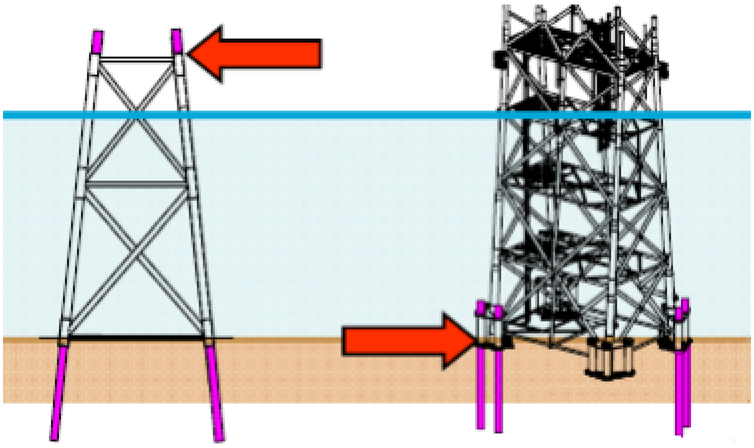

Figure 1.5: A typical schematic example of a jacket installed using post-piling through the legs or sleeves around the legs of the jacket [14].

A pre-piling template is used to install foundation piles for offshore support structures. The use of pre-piling templates is, in particular, beneficial for projects with a large number of support structures. In this case, it is used to install foundation piles of the three-legged jackets. The advantages of a pre-piling template are the reduction in installation time and improved installation accuracy. It is designed to ensure accurate positioning and alignment of the piles. The sleeves of the template provide a predetermined guide for the foundation piles, it also aligns and corrects the position of the piles during pile-driving. Another advantage of a pre-piling template is the reduction of installation time of a support structure. The predefined positions of the foundation piles save time in aligning the piles. Time is also saved by working at different locations at the same time, one ship is installing the foundation piles using the template and another is installing the jacket at a location where the piles are already installed.

First, the pre-piling template is placed on the seabed before pile-driving. When the pre-piling template is lowered onto the seabed, the foundation piles will be driven through the sleeves of the template. During pile driving, the pre-piling template aligns and guides the foundation piles. In Figure 1.6, the pre-piling template built by Huisman is shown. The foundation piles to support the jacket are driven through the sleeves of the pre-piling template and aligned and guided by the centralizers of the template. Foundation piles can be centralized in two different ways. The first option is to guide the pile using rollers. The second is to clamp the pile using a friction pad. In the pre-piling template made by Huisman, the foundation piles are centralized using friction pads. The pre-piling template is equipped with mud mats to prevent sinking into the seabed during pile driving.

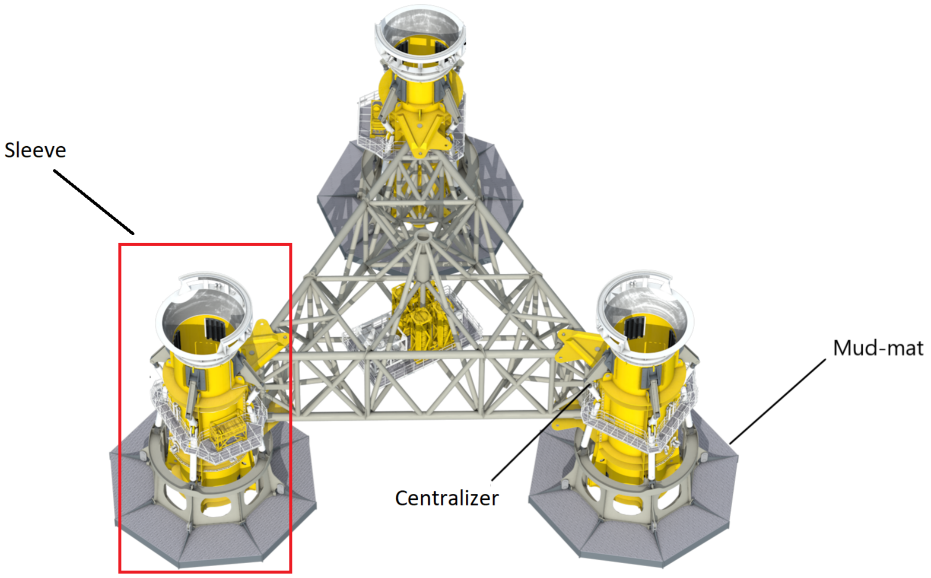

Figure 1.6: A schematic figure of the pre-piling template built by Huisman [15]

Damage was found on the pre-piling template after the installation of the foundation piles. The damage was mainly on the secondary steel at the sleeves of the template. At Huisman, secondary steel is referred to as steel applied outside the main load path such as access platforms, sensor foundations, cable trays, ladders and railings. The cause of the damage is unknown. Following the problem definition, a research question is stated.

1.3.1. Research questions

First, the main research question is presented.

What are the possible reasons for the damage to the secondary steel of the pre-piling template during the installation of the foundation piles?

The main research question can be broken down into three sub-questions:

1. **What possible reasons could result in the pile template interaction causing damage to the pre-piling template?**
2. **How does the current design influence the interaction between the pile and the template?**
3. **How can the design be adjusted so that less damage occurs to the pre-piling template?**

1.4. Methodology and outline of the research

This section describes the approach to answer the research questions.

In the following, a literature review will determine the possible sources of the damage to the pre-piling template. At the end of the literature review, a hypothesis will be stated. Using the literature and the hypothesis, a model will be developed to describe the behavior of the pre-piling template and the pile during pile-driving. The model will be validated and verified to ensure that the simulation results are reliable. When this is done, the simulation results can be analyzed and interpreted. Using the analysis of the results, the hypothesis will be answered as well as the research questions. Finally, conclusions will be drawn to give Huisman recommendations on the design of the template and to address which research has to be done in the future to improve the model and the results. The outline of this thesis is given in Figure 1.7

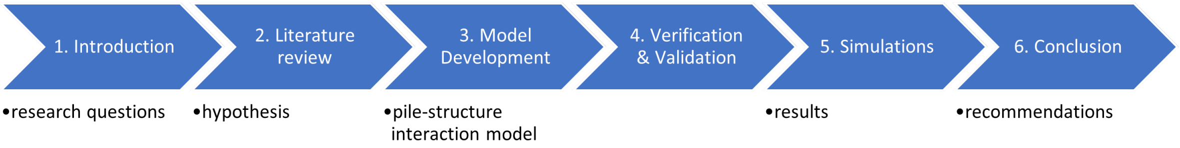

Figure 1.7: The outline of this thesis

2

State-of-the-art in offshore wind installation using a pre-piling template

The previous chapter presents a general introduction to the offshore wind industry and this research. Theoretical background, fundamental definitions, and the theories used within this thesis will be presented regarding the installation of foundation piles using pre-piling templates during the installation of offshore wind turbine parks. This chapter is subdivided into several sections. Section 2.1 will present an overview of the current use of pre-piling templates, in Section 2.2 and Section 2.3 respectively background will be presented about friction models and pile-driving methods. After which, the research-added value will be provided. A hypothesis will be presented to conclude this chapter.

2.1. The use of pre-piling templates

The current use of pre-piling templates is to install the foundation piles of jackets in offshore wind farms. With a growing demand for offshore wind parks supported by jackets, pre-piling templates are becoming increasingly significant. Considering the recentness of pre-piling templates, there is limited research within this field. The research mainly focuses on the template's efficiency during operation, the design of the template, and the study into the hydrodynamic loads acting on the template. As an example, a master thesis is done to investigate the usability of a pre-piling template that could be adjusted so it is applicable to different projects [16].

A pre-piling template is subjected to various forces throughout the installation of foundation piles. Before the foundation piles can be driven into the soil, the pre-piling template needs to be set up on the seabed. A crane on a ship is primarily used to install the template on the seabed. First, the wave zone is traversed by the pre-piling template. A structure is subjected to hydrodynamic forces when lowered through the wave zone because of the impacting waves. In 2023, a study was conducted into the performance of the installation sequence of the template and the hydrodynamic forces acting on the template during the lowering through the wave zone [17].

When lowered onto the seabed, the pre-piling template is corrected and leveled out for the irregularities of the seabed. After this, the foundation piles are installed through the sleeves of the template. Because the foundation can be piles up to 90 m long, they are exposed to hydrodynamic forces such as waves and current loads. Due to the hydrodynamic loads, the foundation piles can sway. A study was done about the influence of swaying piles due to hydrodynamic loading on pre-piling templates prior to pile-driving [18]. Swaying piles can increase the loads on the pre-piling template. The forces due to swaying piles can increase the risk of the template tipping over. To prevent extra loads on the template due to pile swaying, Huisman incorporated an active damping system to prevent the piles from swaying. This excludes pile swaying as a possible cause of the damage done to the template. After the piles are lowered into the template, pile driving can start. During pile driving, vibrations originate from the force of the impact hammer onto the pile. Zwartveld [19] investigated the transfer of vibrations between the pile and template during pile driving. In this thesis, the transverse vibrations are assumed to be radial expansions of longitudinal stress waves induced by the blow of the hammer on top of the pile. The contact between the pile and the template is caused by the misalignment during pile driving. The energy transferred from the pile to the template ranges up to 10% of the hammer input. The results of this study were not validated and the investigated template didn't actively clamp and guide the pile during pile driving. Due to the different interaction between pile and template in the study of Zwartveld and this thesis, the load transfer due to the vibrations can't be compared.

After the foundation piles are installed, the template is removed from the seabed and moved to the next installation location. When removed from the seabed, the template experiences suction forces between the template and the soil. A master thesis is written about the pressure differences that occur during the uplift of mud mats on pre-piling templates [20]. The pressures between the template and the soil can cause peak forces acting on the template. In this study, no research is done on the influence of these forces on the template and if these forces can cause damage to the template.

No research can be found about the interaction between the foundation pile and template during pile driving and actively clamping and guiding the pile doing so. In most pre-piling templates, rollers guide and align the foundation piles during pile driving. Currently, the only known pre-piling template which uses friction pads instead of rollers is the pre-piling template Huisman built. Huisman chose friction pads instead of rollers due to the system's complexity and financial considerations. A few possible causes of the damage to the pre-piling template are hydrodynamic loads during lowering through the wave zone, radial vibrations induced by the impact hammer on the pile, and due to the friction interaction between the piles and the pre-piling template. One big difference between most of the templates and the template of Huisman is the use of friction pads, which are actively clamped on the pile during pile-driving. The pads could significantly contribute to the energy dissipation from the pile to the template. Because pads are rarely used and no research is done on the interaction between friction pads and pre-piling templates, the choice is made to focus on this interaction. However, the other mentioned possible causes can still contribute to the damage.

2.2. Friction model

While no research is done into the interaction between piles and pre-piling templates using friction pads, significant research is done into dynamic friction interaction between surfaces.

The first research on friction in mechanical systems dates to the sixteenth century. In this research, Da Vinci [21] concluded that friction is independent of apparent contact area and the resistance of friction is directly proportional to the applied load. The work done by Da Vinci was validated by Amontons and Coulomb [22] and demonstrated that friction is independent of relative tangential velocity. Amontons and Coulomb came up with the Amontons-Coulomb friction model. This model describes frictional behavior. It also states that the friction coefficient is not always the same for all interacting surfaces. The Amontons-Coulomb model is an efficient model for describing static or stationary situations, but it is unsuitable for dynamic models.

After the research of Coulomb, Dupont et al. [23] investigated that frictional forces are velocity dependent and have elasticity when the surfaces are sticking. Dupont called static friction the presliding regime. Since velocity (Stribeck effect) is one of the diverse phenomena influencing friction, there are different modeling approaches. These modeling approaches can either be analytically or numerically developed. Other friction phenomena are static friction, stick-slip action, frictional lag, pre-sliding displacement, and the break-away force [24]. Friction models can be categorized into two groups, static friction models and dynamic friction models. Static models assume no motion between the two surfaces, the so-called "stick," while dynamic friction models assume a small pre-sliding displacement in the sticking phase [25]. Dynamic friction models also incorporate other friction phenomena [26].

Static friction is quite simplistic and has a low number of involved parameters. They are developed to be computationally efficient and mitigate and eliminate numerical difficulties [24]. Static models are widely used for multi-body dynamic simulations. Some models can even capture dynamic friction phenomena such as stick-slip or hysteresis. Leine et al. [27] introduced alternative friction models to simulate stick-slip vibrations. The friction model consists of ordinary non-stiff differential equations that can be integrated with any Ordinary Differential Equation solver (ODE-solver). Comparison with a smoothing model reveals that this method is more efficient from a computational point of view. The switch model, proposed by Leine et al. [27], uses two differential equations. One set of equations describing the system when in stick and one set of equations describing the system in slip. It uses a slip-to-stick transition condition and a stick-to-slip transition condition to check whether the system is in stick or slip. When a condition is met, the current solver will be stopped and a new solver will begin. One solver solves the equations for the system in stick and the other solver solves the equations for the system in slip. This method will give more insight into which moment the system switches from slip to stick or vice versa.

Dynamic friction models can take more friction phenomena into account, making them more realistic than static friction models. Compared with static friction models, dynamic friction models are more numerically difficult to use and computationally less efficient. Dahl [28] was the first to introduce a dynamical friction model, after which the LuGre [29] model was developed. It is one of the most frequently used dynamic friction models. The LuGre model is a model that can be widely used in different fields of work and is considered the most extensive dynamic friction solution. The model was developed during a cooperation between the Lund and Grenoble universities. The Lugre model is an extension of the earlier mentioned Dahl model. The phenomena captured in the LuGre model are the Stribeck effect, pre-sliding displacement, varying break-away force, and frictional lag. The Lugre model has been widely tested and investigated by different authors. "*The LuGre friction model presents a reasonable trade-off between easiness of implementation, range of modeled frictional phenomena, computational efficiency, and the ability for parameter identification*" [24]. A lot of other dynamic friction models are modifications of the LuGre model, which all focus on a different phenomenon of dynamic friction. For example, Wojtyra [30] analyses the difference between a constant normal load and a non-constant normal load. In this study, it is concluded that the use of non-constant normal force does influence the behavior of the LuGre model a lot.

2.3. Pile-driving

The pile's motions must be modeled to model and determine the interaction behavior between the pile and the template. Pile-driving is a crucial process in the installation of offshore support structures. Modeling pile-driving exists of three parts. The hammer model, the pile, and the soil-pile interaction.

First, the hammer model. There are various ways to hammer a pile into the soil. A great example is impact pile driving, where a mass is lifted and released from a certain height. The resulting impact of the mass on the pile then drives the pile into the soil. Another way of pile-driving is with the use of vibrations. Due to exerted vibrations, the pile penetrates the soil. The impact hammer is currently the most used technique for pile-driving in the installation of offshore wind parks. Historically, the force produced by the hammer is modeled numerically. Smith [31] proposed modeling the parts of the hammer (ram, cushion, and anvil) as lumped masses separated by a spring to represent the cushion between the ram and the pile. After Smith, more complex models were developed. However, Middendorp and van Weele [32] proved that simple hammer models accurately represent the hammer response by comparing field data with different numerical models. An analytical solution can be used if a simple hammer model is used. Randolph and Deeks [33] introduce an analytical model which produces a force-time signal generated by the hammer impact at the head of the pile. This model is also validated with the use of field data and gives an adequate representation of a real impact hammer [33].

To model the pile reaction, one of the most used models is the wave equation method developed by Smith[31]. Using the finite difference method to describe the pile behavior during pile driving. It utilizes a stress wave propagation model to describe the stresses in a pile, the velocity, and the penetration resistance during pile driving. Over the years, researchers added parameters to improve the results of the model. The disadvantage of this model is that it is a relatively complex model with no insight into the system. However, this thesis focuses on the friction interaction between the pile and the pre-piling template. The internal behavior and response of the pile due to the wave-equation model are not in the scope of this thesis. Therefore, the choice is made to assume that the pile is rigid and neglects the wave propagation through the pile due to the impact force of the hammer.

A hammer force over time is applied at the top of the pile to model the impact hammer. The hammer force is calculated using a simplified analytical model of an impact hammer [33]. To model the interaction between the pile and the soil, the LuGre dynamic friction model will be used. The soil-pile interaction is based on friction and resistance, which suits the LuGre model. The LuGre model cannot be used for the interaction between the pile and the template since the normal force between the pile and pad varies [30] and LuGre assumes a constant normal force [29]. The interaction between the pile and template will be a so-called ”static” friction model, which assumes no presliding when in stick. The interaction between the pile and template will be based on the switch model proposed by Leine et al. [27]. It gives more insight into the pile and template interaction and is computationally more efficient [24].

2.4. Research added value

This chapter discusses the research on installing foundation piles in the offshore wind industry. However, little literature is written about installing offshore wind support structures using pre-piling templates, mainly focusing on the interaction between foundation piles and pre-piling templates during pile driving. Researching the impact of friction pads on the interaction between a foundation pile and a pre-piling template is new in the field. Therefore, in combination with the problem statement and the existing literature, a hypothesis is formulated.

In Figure 2.1, a detailed blueprint of one of the sleeves of the pre-piling template can be seen. In the close-up of the sleeve, a detailed blueprint of the centralizers can be seen. The function of the centralizers is to align and guide the foundation piles during pile driving. At each sleeve, four centralizers actively align the foundation piles. The piles are held with friction pads at the end of each centralizer. Hydraulic cylinders control the centralizers. During pile driving, the pads apply a pretension force at the pile to hold the pile in the center of the sleeve. Due to friction, the pads want to stick to the pile during pile driving and move along with the pile. The orientation of the current upper centralizers and the friction causes a rotation of the centralizers and the pads into the pile. This leads to an increase in the friction force between the pile and the pads. This causes the pile to penetrate the soil less and increases the energy dissipation into the template. This theory leads to the hypothesis:

The current design of the upper centralizers causes an increase of the peak normal force and thus of the frictional force between the pile and pads while hammering the pile through the pre-piling template resulting in damage to the secondary steel of the pre-piling template.

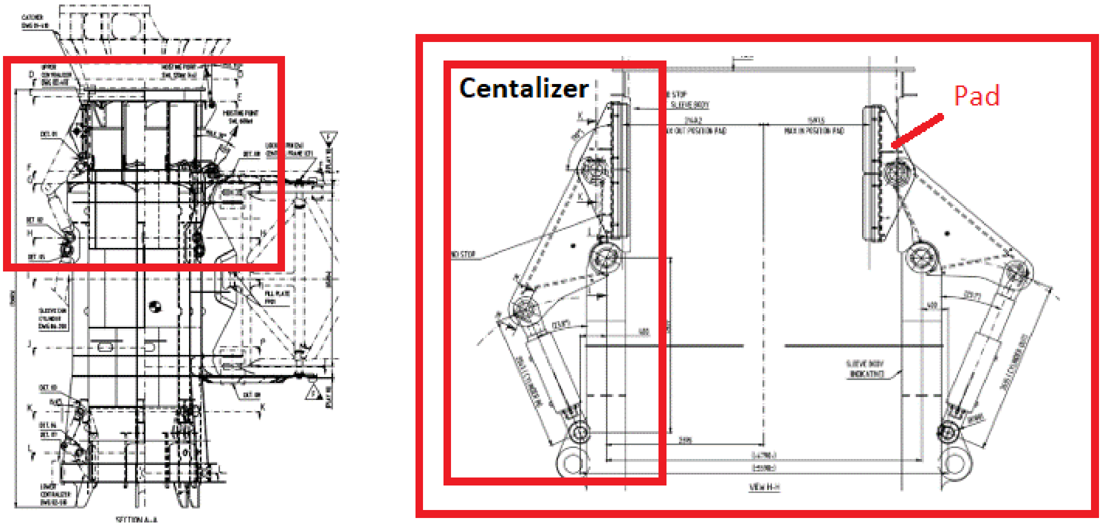

Figure 2.1: A detailed figure of the sleeve of the pre-piling template and a close-up of the centralizers [15].

3

A numerical model that describes the pile-template interaction during offshore pile driving

This chapter presents a model that describes the interaction between the foundation pile and the pre-piling template during offshore pile driving. In Section 3.1, first the modeling strategy is presented, after which the scope and limitations of the model are given to explain how the model addresses the thesis objectives and helps to answer the research questions. Section 3.1 concludes with an overview of the assumptions made for the model. Section 3.2 presents a detailed overview of the numerical model.

3.1. The description of the model

3.1.1. Approach

To describe the interaction of the upper centralizer and pile during pile driving, the model is divided into three sub-models:

1. A model to calculate the hammer force on the pile during pile driving;
2. A model to represent the soil-pile interaction;
3. A model to describe the pile-template interaction.

The first two models will give an external force over time, which will be applied to the pile. The pile will only have one Degree of Freedom (DoF) in vertical direction. The upper centralizer will also have one DoF, rotating around a point. These two degrees of freedom will be expressed in a set of equations of motion. These equations of motion can be rewritten into second-order differential equations. Before these equations can be solved they need to be rewritten into an equivalent system of first-order equations. These equations can be solved using an internal ODE (ordinary differential equation) Matlab solver. This solver is time-based. Since the complexity of the number of states is limited in this research so it is expected that the system won't be 'stiff'. This means that the internal step size of the solver will not be forced down to small step sizes, which can lead to the failure of the integration. For a non-stiff system, the ODE45 solver is advised [34]. If the system turns out stiff anyway, another solver can be chosen.

3.1.2. Scope and limitations

The scope of the model is to describe and calculate the behavior of the pile and the upper centralizer while pile driving. The behavior of the pile and upper centralizer will be expressed in acceleration, velocity, and displacement in the desired degrees of freedom. To calculate the behavior of the pile and the upper centralizer, the soil-pile interaction and hammer force need to be calculated as input.

The model is limited by using rigid bodies. This results in the motion of whole structures and not internally in every part. No conclusion can be made about the internal vibration and energy losses in the pile, pad, and pre-piling template. Also, when hammering a pile into the soil a propagating wave through the pile is initiated due to the force exerted on the top of the pile. This causes displacements in the pile in axial, circumferential, and radial directions. These displacements are not considered in this model [35]. The model used to calculate the hammer force has its limitations. The model uses a lumped ram mass rather than a distributed mass, which will influence the force's response at the pile head. However, in the literature, it is stated that the curve of the force over time is smoother but in other respects identical [33].

The limitation of using the LuGre [29] friction model is the dependency on determining different friction parameters. Those will not be available in every case. The LuGre model is a simplified model. With the complexes of soil mechanics, this could lead to different results. The LuGre model is known to have a slight additional drift after each cycle [36].

3.1.3. Assumptions

A rigid pile, pad, and upper centralizer are assumed to make the model simpler and the calculations quicker. An equivalent radial pile stiffness is introduced to represent the interaction between the pile and pad. This stiffness is calculated using the Finite element model software ANSYS.

The displacement of the pile is only assumed in vertical direction to generate an equal load on all the pads. The hydrodynamic loads on the pile and template are neglected because the pile can only move in vertical direction. Hydrodynamic loads will lead to an off-lead and swaying of the pile, which leads to an unequal load on the pads. However, since the pile can only move in vertical direction this will not happen. The interest of this thesis is mainly focused on the pure lateral interaction between the pile and the pre-piling template. Further research could investigate the results by adding non-rigid elements to the system. Also, adding more degrees of freedom to the pile could be investigated. Then it is also possible to look into the effects of hydrodynamic loads. For the derivations of Subsection 3.2.3, the small angle approximation is used because the rotational degree of freedom $\theta \ll 1$ so the following equations are used. In Figure 3.1 a schematic overview of the system with all its components is given. Here the coordinate system is also defined. The z-direction is positive downwards and the y-direction is to the right. The angle θ is determined positive anti-clockwise.

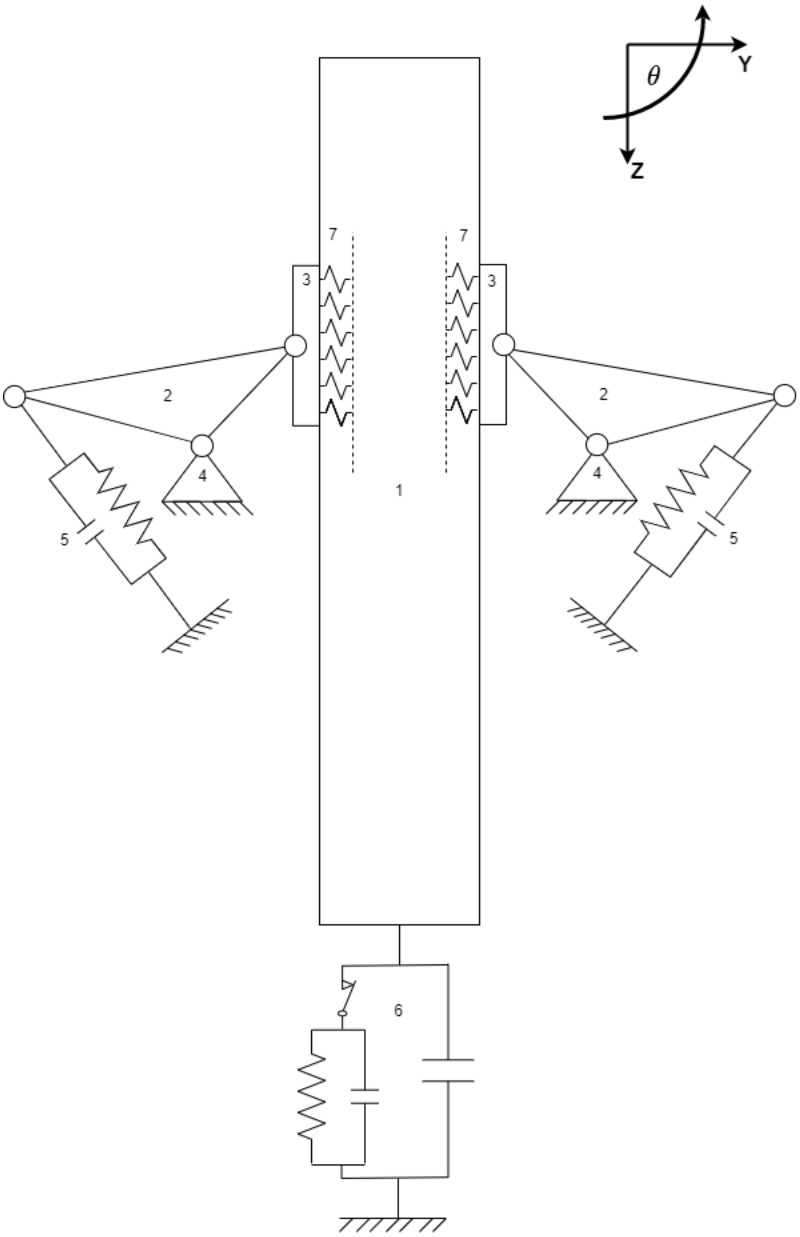

Figure 3.1: Schematic overview of the model. 1. Rigid Pile; 2. Rigid upper centralizer; 3. Rigid pad; 4. Supporting hinge; 5. Spring-damper system representing hydraulic cylinder; 6. System of LuGre element with plastic damping which represents soil-pile interaction; 7. Radial pile stiffness.

3.2. An overview of the model

3.2.1. Modeling of the impact of the hammer on the pile

One of the options to install a foundation pile into the seabed is using an impact hammer. An impact hammer uses a heavy ram that is dropped from a height. Due to the impact of this ram, the pile is driven into the soil a certain amount. In this thesis, a Menck 1900s hammer is used since this was the hammer used during the installation of the wind turbine park. In Figure 3.2a, a typical layout of an impact hammer is shown. To calculate the force of the hammer on the pile a simplified analytical model [33] is introduced which can be seen in Figure 3.2b. The ram is assumed as a lumped mass m_r. The pile is modeled as a dashpot, of impedance Z and the cushion has a stiffness k_c. The input of the model is v_0. This is the impact speed of the hammer when hitting the pile.

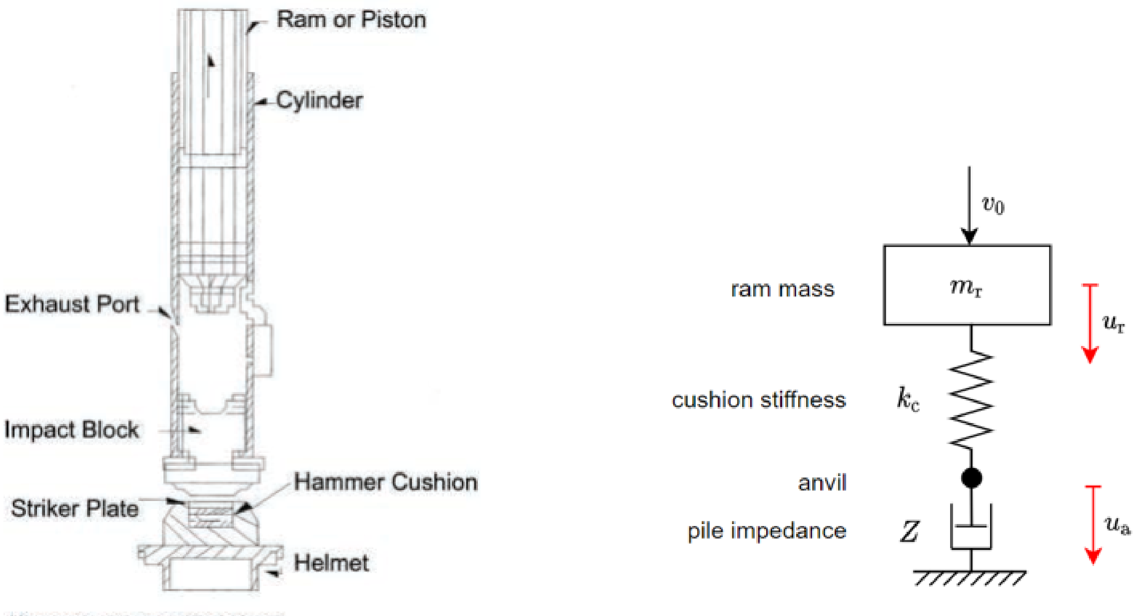

(a) Schematic overview of a typical impact hammer [37].

(b) Schematic representation of the analytical model to calculate the force of the hammer at the top of the foundation pile [33].

Figure 3.2: A typical impact hammer and an analytical representation of an impact hammer

The pile impedance is given by Equation 3.1, where c is the wave speed of steel and EA is the cross-sectional rigidity of the pile. The impact speed of the ram is calculated using the energy conservation law. The ram is dropped from a certain height. The height is determined by the maximal energy capacity of the hammer E_{hammer}, in this case, 1900 kJ. Using the maximum energy, the maximal impact speed can be calculated using kinetic energy. See Equation 3.2.

$$Z = \frac{EA}{c} \tag{3.1}$$

$$v_0 = \sqrt{\frac{2E_{hammer}}{m_{ram}}} \tag{3.2}$$

The equations of motion of the analytical model are defined in Equation 3.3, where there are two degrees of freedom: The displacement of the ram, u_r, and the displacement of the anvil, u_a. Using dimensionless variables dimensionless stiffness $\bar{k}_c$ and time $\bar{t}$ can be introduced, see Equation 3.4 and Equation 3.5.

$$\begin{aligned} m_{\mathrm{r}}\ddot{u}_{\mathrm{r}} + k_c\left(u_{\mathrm{r}} - u_{\mathrm{a}}\right) = 0 \\ Z\dot{u}_{\mathrm{a}} - k_c\left(u_{\mathrm{T}} - u_{\mathrm{a}}\right) = 0 \end{aligned} \tag{3.3}$$

$$\bar{k}_c = \frac{m_r}{Z^2} k_c \tag{3.4}$$

$$\bar{t} = \frac{Z}{m_r} t \tag{3.5}$$

After the dimensionless time $\bar{t}$ and stiffness $\bar{k}_c$ are derived the dimensionless force $\bar{F}_c$ can be calculated using Equation 3.6.

$$\begin{aligned} \bar{F} &= e^{-\frac{1}{2}\bar{k}_c \bar{t}} \frac{\bar{k}_c}{\mu} \sin(\mu \bar{t}) \\ \mu &= \sqrt{\bar{k}_c - \frac{1}{4}\bar{k}_c^{\,2}} \end{aligned} \tag{3.6}$$

Now the dimensionless force $\bar{F}$ is known, it can be derived further into a force over time using the impact velocity v_0 and the impedance Z (Equation 3.8). The dimensionless time $\bar{t}$ and the normal time t can be related using Equation 3.7. Now the hammer force $F(t)$ over time is known it can be used in the final model to represent the impact of an impact hammer onto the top of the pile.

$$\bar{t} = \frac{Z}{m_r} t \tag{3.7}$$

$$F(t) = Z v_0 \overline{F}(t) \tag{3.8}$$

3.2.2. Soil-pile interaction

The LuGre [29] friction model is used to represent the interaction between the pile and the soil. LuGre [29] is a dynamic friction model based on the principle of bristle contact. The interaction between the pile and soil is modeled as elastic bristles with damping. In Figure 3.3a the bristles between the two surfaces can be seen. The average bristle deflection z is used to calculate the friction force between the pile and the soil. In Figure 3.3b, the LuGre element shown in Figure 3.3a, is simplified as a spring-damper friction element and placed at the bottom of the pile. See the red circle in Figure 3.3b.

The average bristle deformation is modeled by the first-order differential Equation 3.9, where v is the relative velocity between the two surfaces. In this case, that is the relative velocity between the pile and the soil. Since the soil is assumed not to be moving, v is equal to the velocity of the pile. Hence $\dot{z}_{pile}$ can be substituted into Equation 3.9 resulting in Equation 3.10.

$$\dot{z}_{lugre} = v - z_{lugre} \frac{\sigma_0 |v|}{G(v)} \tag{3.9}$$

$$\dot{z}_{lugre} = \dot{z}_{pile} - z_{lugre} \frac{\sigma_0 |\dot{z}_{pile}|}{G(\dot{z}_{pile})} \tag{3.10}$$

The function $G(\dot{z}_{pile})$ allows the LuGre model to accommodate a higher static friction force than the dynamic friction coefficient. It is describing the Stribeck effect [38], which is the decrease of the friction coefficient with an increasing sliding velocity, where F_C is the kinetic friction force, F_S is the maximum static friction force and ϑ the Stribeck velocity. The kinetic friction force and maximum friction force of the soil are known from soil research at the site of installation.

$$G(\dot{z}_{pile}) = F_\mathrm{C} + (F_\mathrm{S} - F_\mathrm{C})\, e^{-(\dot{z}_{pile}/\vartheta)^2} \tag{3.11}$$

Finally, the LuGre friction force is given by Equation 3.12. Here σ_0 is the soil stiffness coefficient, σ_1 the soil damping coefficient and σ_2 is the viscous friction coefficient. All the soil data is known from site research. Since the soil force F_{soil} is calculated using a first-order differential equation, it will be one of the states in the solver. At every time step, a new soil force will be calculated. The states can be seen in Subsection 3.2.3 in Equation 3.26 and Equation 3.41.

$$F_{soil} = \sigma_0 z_{lugre} + \sigma_1 \dot{z}_{lugre} + \sigma_2 \dot{z}_{pile} \tag{3.12}$$

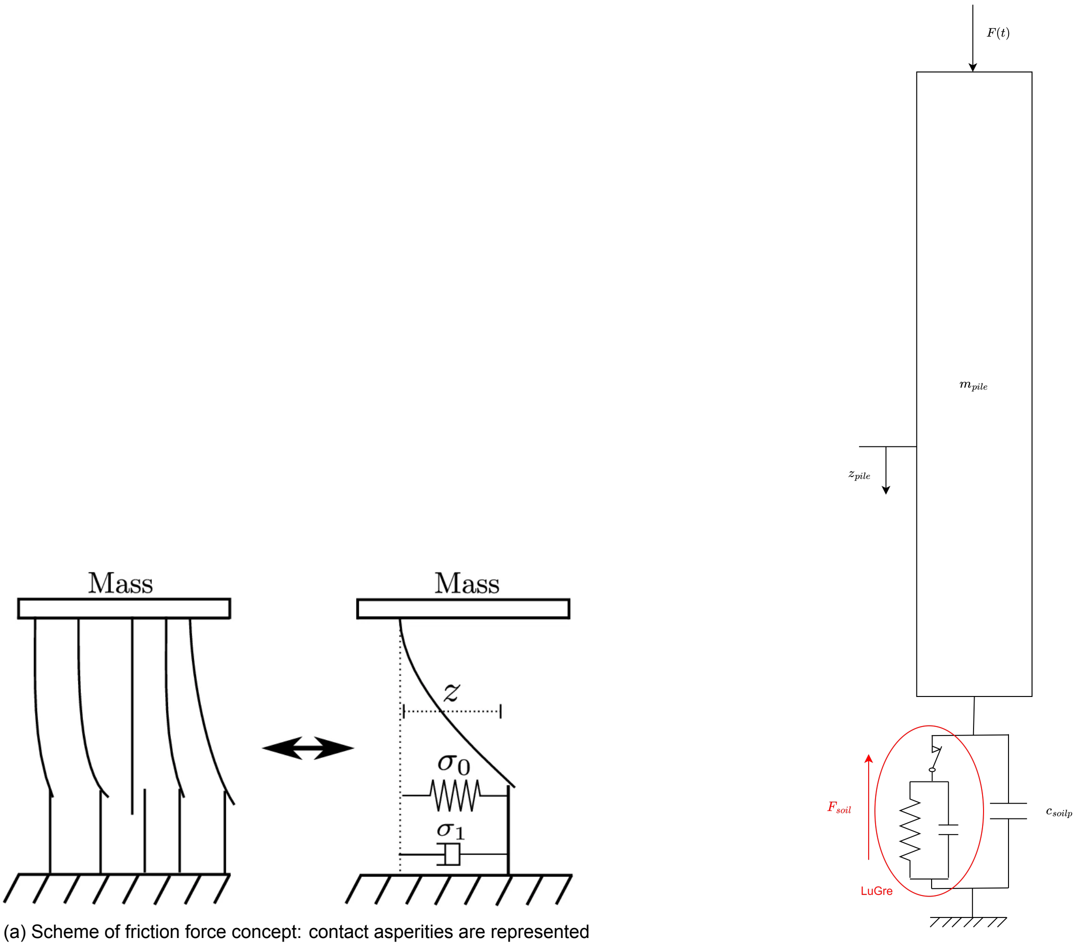

(a) Scheme of friction force concept: contact asperities are represented as elastic bristles with damping. The LuGre model is used, where the friction force is determined considering an average bristle deflection z [39]

(b) Schematic figure of how the LuGre element acts on the pile, the LuGre element is applied at the bottom of the pile. See the red circle.

Figure 3.3: A schematic overview of the LuGre model and the LuGre model applied at the bottom of the pile.

3.2.3. Pile-template stick-slip interaction

The interaction between the pile and the pre-piling template is a friction model based on a switching stick-slip motion [27]. A stick-slip motion occurs between two surfaces in contact, in this case, the pad of the upper centralizer and the pile. When there is stick between the pile and the pad, there is no relative velocity between them. But when slip occurs, there is a relative velocity between the pile and pad. The pile is initially at rest and the pad is applying a constant pretension on the pile to hold it in place. When the pile wants to move down in the z-direction, due to the hammer acting as a force on the pile, the static friction between the pile and the pad induced by the pretension prevents a sliding motion between the pile and the pad. They stick together and there will be no relative motion. When the force between the pile and pad is exceeding the static friction, the pile and pad will slip and there will be a relative velocity between the pad and pile. The pile slows down due to the force of the soil and the kinetic friction between the pile and the pad. If the relative velocity between the pile and pad becomes zero, they will again stick to each other.

In Figure 3.4, the degrees of freedom for the pile and the triangle can be seen. These are respectively z_{pile} and θ. Where z_{pile} is the vertical displacement of the pile and θ is the rotation of the upper centralizer (referred to in the equations and figures as a triangle) around fixed point C. There are in total four upper centralizers interacting with the pile. In the equations, upper centralizer forces acting on the pile are multiplied by four and the other way around pile forces acting on one upper centralizer are divided by four.

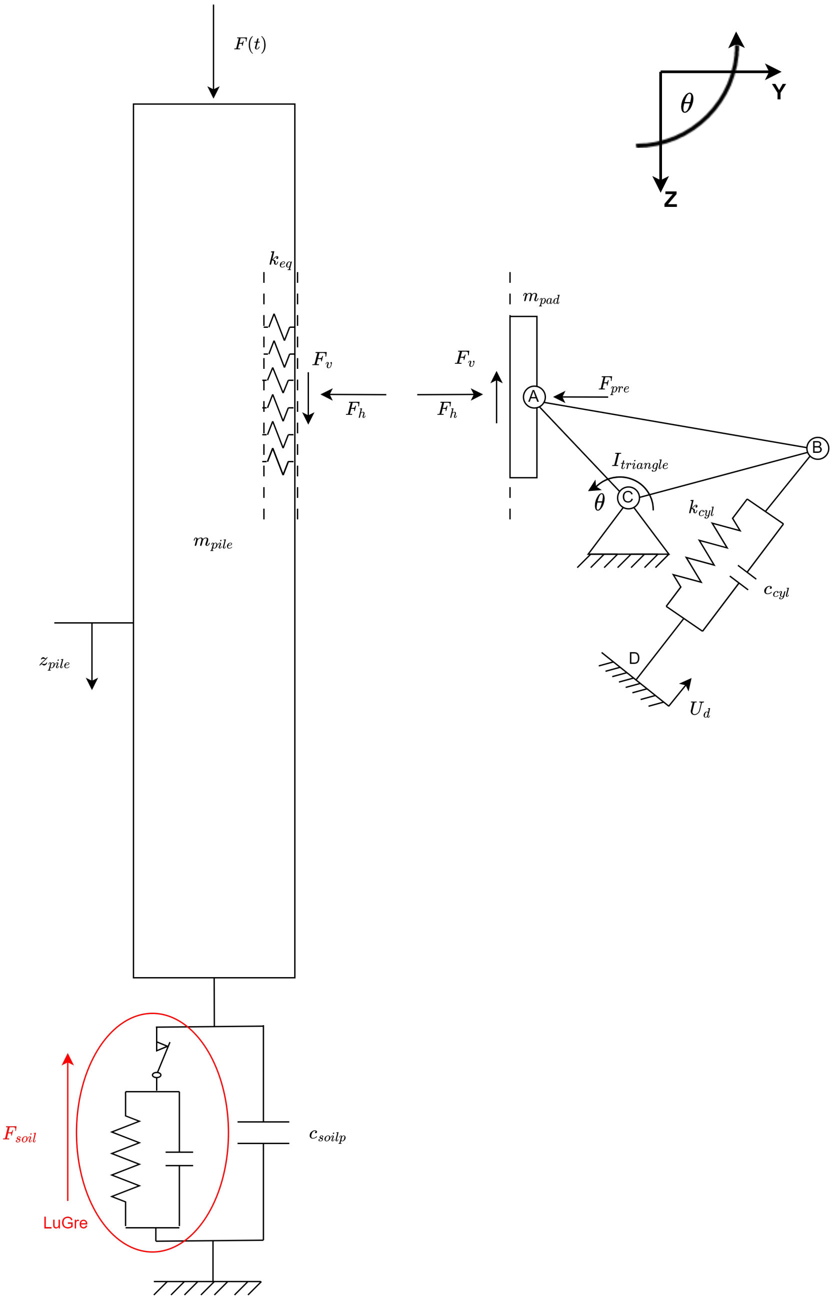

Figure 3.4: The interaction between pile and upper centralizer in slip

Consider the situation as shown in Figure 3.4. As the system has only two degrees of freedom, two equations of motion are required to solve the system. Considering the balance of moments around point C, the equation of motion of the rigid upper centralizer can be found as Equation 3.13.

$$I_{triangle}\ddot{\theta} = M_v + M_{pre} + M_{pad} - M_{cyl} - M_h \tag{3.13}$$

Here, θ describes the rotation about point C and $I_{triangle}$ is the mass moment of inertia of the triangle, derived in Appendix D. Furthermore, M_v, M_{cyl}, M_{pre}, M_h and M_{pad} are the moments around point c due to the force F_v, the force F_{pre}, the mass of the pad, the elongation of k_{cyl} and elongation rate of c_{cyl} and the force F_h. The equations for M_v, M_h and M_{pad} follow from the moment about point C and respectively read:

$$M_v = F_v L_\beta cos(\beta) \tag{3.14}$$

$$\begin{aligned} M_h &= F_h L_\beta sin(\beta) \\ &= k_{eq} \theta L_\beta^2 sin(\beta)^2 \end{aligned} \tag{3.15}$$

$$M_{pad} = m_{pad} g L_\beta cos(\beta) \tag{3.16}$$

More detailed derivations of the moments can be found in Appendix A.1.1 to Appendix A.1.3. The moment M_{cyl} due to the elongation of k_{cyl} and the elongation rate of c_{cyl} is described in Equation 3.17.

$$\begin{aligned} M_{cyl} &= k_{cyl}(U_d - L_\alpha \theta) L_\alpha + c_{cyl}(\dot{U}_d - L_\alpha \dot{\theta}) L_\alpha \\ &= k_{cyl}(U_d - L_\alpha \theta) L_\alpha - c_{cyl} L_\alpha^2 \dot{\theta} \end{aligned} \tag{3.17}$$

The more detailed derivation of M_{cyl} can be found in Appendix A.1.2. U_d is the displacement of point D to compensate for the initial rotation of the upper centralizer due to the pretension applied at point A. The detailed derivation of U_d can be found in Appendix A.1.4.

To align the pile and keep it centered, the upper centralizer applies a pretension force at point A, expressed as F_{pre}. The moment M_{pre} around point C due to F_{pre} is described in Equation 3.18.

$$M_{pre} = F_{pre} L_\beta \sin(\beta) \tag{3.18}$$

The arm of M_{pre} is the same as M_h derived in Appendix A.1.1. Substituting Equation 3.14 to Equation 3.18 into Equation 3.13, the equation of motion of the rotation around point C can be written as Equation 3.19.

$$\begin{aligned} I_{triangle}\ddot{\theta} = {} & F_v L_\beta cos(\beta) + F_{pre} L_\beta \sin(\beta) + m_{pad} g L_\beta cos(\beta) \\ & - k_{cyl}(U_d - L_\alpha \theta) L_\alpha + c_{cyl} L_\alpha^2 \dot{\theta} - k_{eq} \theta L_\beta^2 sin(\beta)^2 \end{aligned} \tag{3.19}$$

The second equation of motion is related to the degree of freedom, z_{pile}, and follows from the motion of the rigid pile only in the z-direction. From Figure 3.4, the equation of motion is described as Equation 3.20.

$$m_{pile}\ddot{z}_{pile} + c_{soilp}\dot{z}_{pile} = F(t) + m_{pile} g + 4F_v - F_{soil} \tag{3.20}$$

Here, F(t) is the external force of the hammer, F_{soil} is the external force of the soil calculated using the LuGre model from Subsection 3.2.2, c_{soilp} represents the plastic damping of the soil and F_v is the vertical force acting on the pile due to the interaction with the upper centralizer.

Stick

When the system is in stick regime, there is no relative movement between the pad and the pile. If the pile moves the upper centralizer will also move. In stick, the relation between the motions around point C and the motions of the pile is constrained. The constraint equations which describe this relation can be seen in Equation 3.21. This constrained motion means that one of the degrees of freedom will disappear. The equations of motion can be combined using F_v, which is an unknown force in stick, and the constraint Equation 3.21.

$$\theta = \frac{z_{pile}}{L_\beta \cos(\beta)}, \qquad \dot{\theta} = \frac{\dot{z}_{pile}}{L_\beta \cos(\beta)}, \qquad \ddot{\theta} = \frac{\ddot{z}_{pile}}{L_\beta \cos(\beta)} \tag{3.21}$$

First, F_v can be described by rewriting Equation 3.20 into Equation 3.22 and substituted into the equation of motion of the upper centralizer Equation 3.19. The new equation of motion is described as Equation 3.23

$$F_v = \frac{1}{4}(m_{pile}(\ddot{z}_{pile} - g) + c_{soilp}\dot{z}_{pile} + F_{soil} - F(t)) \tag{3.22}$$

$$\begin{aligned} I_{triangle}\ddot{\theta} &= F_v L_\beta cos(\beta) + F_{pre} L_\beta \sin(\beta) + m_{pad} g L_\beta cos(\beta) - k_{cyl}(U_d - L_\alpha \theta)L_\alpha \\ &\qquad + c_{cyl} L_\alpha^2 \dot{\theta} - k_{eq}\theta L_\beta^2 sin(\beta)^2 \\ &= \frac{1}{4}(F(t) + m_{pile}(\ddot{z}_{pile} - g) - F_{soil} - c_{soilp}\dot{z}_{pile})L_\beta cos(\beta) + F_{pre} L_\beta \sin(\beta) \\ &\qquad + m_{pad} g L_\beta cos(\beta) - k_{cyl}(U_d - L_\alpha \theta)L_\alpha + c_{cyl} L_\alpha^2 \dot{\theta} - k_{eq}\theta L_\beta^2 sin(\beta)^2 \end{aligned} \tag{3.23}$$

Now Equation 3.23 is defined, the constraint Equation 3.21 can be substituted into it. A new equation of motion expressed in z_{pile} is made (Equation 3.25). Equation 3.25, is derived when moving all acceleration parts of the equation to the left-hand side of Equation 3.24. When the $\ddot{z}_{pile}$, $\dot{z}_{pile}$ and z_{pile} are filled into Equation 3.22, F_v can be calculated.

$$\begin{aligned} I_{triangle}\frac{\ddot{z}_{pile}}{L_\beta \cos(\beta)} &= \frac{1}{4}(m_{pile}(\ddot{z}_{pile} - g) + c_{soilp}\dot{z}_{pile} + F_{soil} - F(t))L_\beta cos(\beta) \\ &\quad + k_{cyl}(U_d - L_\alpha \frac{z_{pile}}{L_\beta \cos(\beta)})L_\alpha - c_{cyl} L_\alpha^2 \frac{\dot{z}_{pile}}{L_\beta \cos(\beta)} - k_{eq}\frac{z_{pile}}{L_\beta \cos(\beta)} L_\beta^2 sin(\beta)^2 \end{aligned} \tag{3.24}$$

$$\begin{aligned} \ddot{z}_{pile}(\frac{I_{triangle}}{L_\beta cos(\beta)} - \frac{1}{4}m_{pile} L_\beta cos(\beta)) &= \frac{1}{4}(c_{soilp}\dot{z}_{pile} + F_{soil} - F(t) - m_{pile} g)L_\beta cos(\beta) \\ &\quad + k_{cyl}(U_d - L_\alpha \frac{z_{pile}}{L_\beta \cos(\beta)})L_\alpha - c_{cyl} L_\alpha^2 \frac{\dot{z}_{pile}}{L_\beta \cos(\beta)} - k_{eq}\frac{z_{pile}}{L_\beta \cos(\beta)} L_\beta^2 sin(\beta)^2 \end{aligned} \tag{3.25}$$

Now the equation of motion in stick is known. The equation can be rewritten into a first-order differential equation as input for the ODE solver in Matlab using Equation 3.26. First, move everything from the left-hand side of Equation 3.25 to the right except the acceleration of the pile, $\ddot{z}_{pile}$, see Equation 3.27.

$$y = \begin{bmatrix} y_1 \\ y_2 \\ y_3 \end{bmatrix} = \begin{bmatrix} z_{pile} \\ \dot{z}_{pile} \\ z_{lugre} \end{bmatrix}, \qquad \dot{y} = \begin{bmatrix} \dot{y}_1 \\ \dot{y}_2 \\ \dot{y}_3 \end{bmatrix} = \begin{bmatrix} y_2 \\ \ddot{z}_{pile} \\ \dot{z}_{lugre} \end{bmatrix} \tag{3.26}$$

$$\begin{aligned} \ddot{z}_{pile} = &\frac{\frac{1}{4}(c_{soilp}\dot{z}_{pile} + F_{soil} - F(t) - m_{pile} g)L_\beta cos(\beta) + k_{cyl}(U_d - L_\alpha \frac{z_{pile}}{L_\beta \cos(\beta)})L_\alpha}{(\frac{I_{triangle}}{L_\beta cos(\beta)} - \frac{1}{4}m_{pile} L_\beta cos(\beta))} \\ &\qquad \frac{-c_{cyl} L_\alpha^2 \frac{\dot{z}_{pile}}{L_\beta \cos(\beta)} - k_{eq}\frac{z_{pile}}{L_\beta \cos(\beta)} L_\beta^2 sin(\beta)^2}{(\frac{I_{triangle}}{L_\beta cos(\beta)} - \frac{1}{4}m_{pile} L_\beta cos(\beta))} \end{aligned} \tag{3.27}$$

Then substitute z_{pile} and $\dot{z}_{pile}$ by respectively y_1 and y_2 and in Equation 3.27.

$$\ddot{z}_{pile} = \frac{\frac{1}{4}(c_{soilp}y_2 + F_{soil} - F(t) - m_{pile}g)L_\beta cos(\beta) + k_{cyl}(U_d - L_\alpha \frac{y_1}{L_\beta \cos(\beta)})L_\alpha}{(\frac{I_{triangle}}{L_\beta cos(\beta)} - \frac{1}{4}m_{pile}L_\beta cos(\beta))} \frac{-c_{cyl}L_\alpha^2 \frac{y_2}{L_\beta \cos(\beta)} - k_{eq}\frac{y_1}{L_\beta \cos(\beta)}L_\beta^2 sin(\beta)^2}{(\frac{I_{triangle}}{L_\beta cos(\beta)} - \frac{1}{4}m_{pile}L_\beta cos(\beta))} \tag{3.28}$$

The input of the solver is $\dot{y}(t, y)$ calculated with the initial values Equation 3.29 when the simulation starts or with the output of the last time step of the slip solver when changing from slip to stick Equation 3.30. The output of the solver is $y(t)$. Every time step the input values of the solver are calculated with the output of the previous time step.

$$y(t=0) = \begin{bmatrix} y_1(t=0) \\ y_2(t=0) \\ y_3(t=0) \end{bmatrix} = \begin{bmatrix} z_{pile}(t=0) \\ \dot{z}_{pile}(t=0) \\ z_{lugre}(t=0) \end{bmatrix} \tag{3.29}$$

$$y(t=end_{slip}) = \begin{bmatrix} y_1(t=end_{slip}) \\ y_2(t=end_{slip}) \\ y_3(t=end_{slip}) \end{bmatrix} = \begin{bmatrix} z_{pile}(t=end_{slip}) \\ \dot{z}_{pile}(t=end_{slip}) \\ z_{lugre}(t=end_{slip}) \end{bmatrix} \tag{3.30}$$

The motions of the upper centralizer can ultimately be calculated with the output of the stick solver using Equation 3.21, resulting in Equation 3.31.

$$\theta(t) = \frac{z_{pile}(t)}{L_\beta \cos(\beta)}, \quad \dot{\theta}(t) = \frac{\dot{z}_{pile}(t)}{L_\beta \cos(\beta)}, \quad \ddot{\theta}(t) = \frac{\ddot{z}_{pile}(t)}{L_\beta \cos(\beta)} \tag{3.31}$$

Stick-to-slip transition

The stick-to-slip transition occurs when the absolute value of F_v (Equation 3.22) is greater than or equal to the critical friction force F_{crit}. The critical friction force can't let the pad stick to the pile anymore. The condition when the transition happens is stated in Equation 3.32.

$$|F_v| \geq F_{crit} \tag{3.32}$$

The horizontal force F_h and the static friction coefficient determine the critical friction force, see Equation 3.34. The horizontal force is the force F_h between the pad and pile, which is calculated by the rotation of the upper centralizer θ and the equivalent stiffness of the pile k_{eq} (Equation 3.33). The equivalent stiffness of the pile is calculated using FEA, see Appendix B.

$$F_h = k_{eq}L_\beta\theta sin(\beta) \tag{3.33}$$

$$F_{crit} = F_h\mu_s \tag{3.34}$$

Slip

For slip, the equations of motion: Equation 3.19 and Equation 3.20 are used. For slip F_v is known and described as Equation 3.35. The direction of the vertical force is dependent on the direction of the relative speed between the pile and the pad. The magnitude of the force is dependent on the horizontal force F_h and the dynamic friction coefficient μ_d.

$$F_v = F_{fric}sgn|\dot{z}_{pile} - \dot{z}_{pad}| \text{ where, } F_{fric} = F_h\mu_d \tag{3.35}$$

Based on Equation 3.21, $\dot{z}_{pad}$ can be rewritten as:

$$\dot{z}_{pad} = \dot{\theta} L_\beta \cos(\beta) \tag{3.36}$$

Substituting Equation 3.35 into Equation 3.19 and Equation 3.20 gives the equations of motion in slip for the pile. The rotation around point C is described in Equation 3.37 and Equation 3.38, Where F_h is described by Appendix A.11. the derivation of F_h can be found in Appendix A.1.3.

$$m_{pile}\ddot{z}_{pile} + c_{soilp}\dot{z}_{pile} = F(t) + m_{pile}g - F_h \mu_d sgn|\dot{z}_{pile} - \dot{\theta} L_\beta \cos(\beta)| - F_{soil} \tag{3.37}$$

$$\begin{aligned} I_{triangle}\ddot{\theta} = {} & F_h \mu_d sgn|\dot{z}_{pile} - \dot{\theta} L_\beta \cos(\beta)| L_\beta cos(\beta) + F_{pre} L_\beta \sin(\beta) \\ & + m_{pad} g L_\beta cos(\beta) - k_{cyl}(U_d - L_\alpha \theta) L_\alpha + c_{cyl} L_\alpha^2 \dot{\theta} - k_{eq} \theta L_\beta^2 sin(\beta)^2 \end{aligned} \tag{3.38}$$

Substituting F_h (Appendix A.11) into Equation 3.20 and Equation 3.38 gives Equation 3.39 and Equation 3.40.

$$m_{pile}\ddot{z}_{pile} + c_{soilp}\dot{z}_{pile} = F(t) + m_{pile}g - k_{eq}\theta L_\beta^2 sin(\beta)^2 mu_d sgn|\dot{z}_{pile} - \dot{\theta} L_\beta \cos(\beta)| - F_{soil} \tag{3.39}$$

$$\begin{aligned} I_{triangle}\ddot{\theta} = {} & k_{eq}\theta L_\beta^2 sin(\beta)^2 \mu_d sgn|\dot{z}_{pile} - \dot{\theta} L_\beta \cos(\beta)| L_\beta cos(\beta) + F_{pre} L_\beta \sin(\beta) \\ & + m_{pad} g L_\beta cos(\beta) - k_{cyl}(U_d - L_\alpha \theta) L_\alpha + c_{cyl} L_\alpha^2 \dot{\theta} - k_{eq} \theta L_\beta^2 sin(\beta)^2 \end{aligned} \tag{3.40}$$

Now the equation of motion in slip is known. The equations can be rewritten into first-order differential equations as input for the ODE solver in Matlab using Equation 3.41. This is analogous to rewriting the slip equations of motion into ODE. First, move everything from the left-hand side of Equation 3.37 to the right except the acceleration of the pile, $\ddot{z}_{pile}$, see Equation 3.42. The same can be done for the equation of motion of the upper centralizer. See Equation 3.43.

$$y = \begin{bmatrix} y_1 \\ y_2 \\ y_3 \\ y_4 \\ y_5 \end{bmatrix} = \begin{bmatrix} z_{pile} \\ \dot{z}_{pile} \\ \theta \\ \dot{\theta} \\ z_{lugre} \end{bmatrix}, \quad \dot{y} = \begin{bmatrix} \dot{y}_1 \\ \dot{y}_2 \\ \dot{y}_3 \\ \dot{y}_4 \end{bmatrix} = \begin{bmatrix} y_2 \\ \ddot{z}_{pile} \\ y_4 \\ \ddot{\theta} \\ \dot{z}_{lugre} \end{bmatrix} \tag{3.41}$$

$$\ddot{z}_{pile} = \frac{F(t) + m_{pile}g - F_h \mu_d sgn|\dot{z}_{pile} - \dot{\theta} L_\beta \cos(\beta)| - F_{soil} - c_{soilp}\dot{z}_{pile}}{m_{pile}} \tag{3.42}$$

$$\begin{aligned} \ddot{\theta} = {} & \frac{F_h \mu_d sgn|\dot{z}_{pile} - \dot{\theta} L_\beta \cos(\beta)| L_\beta cos(\beta) + F_{pre} L_\beta \sin(\beta) + m_{pad} g L_\beta cos(\beta)}{I_{triangle}} \\ & \frac{-k_{cyl}(U_d - L_\alpha \theta) L_\alpha + c_{cyl} L_\alpha^2 y_4 - k_{eq} y_3 L_\beta^2 sin(\beta)^2}{I_{triangle}} \end{aligned} \tag{3.43}$$

Then substitute z_{pile}, $\dot{z}_{pile}$, θ and $\dot{\theta}$ by respectively y_1, y_2, y_3 and y_4 in Equation 3.42 and Equation 3.43. See Equation 3.44 and Equation 3.45.

$$\ddot{z}_{pile} = \frac{F(t) + m_{pile}g - F_h \mu_d sgn|y_2 - y_4 L_\beta \cos(\beta)| - F_{soil} - c_{soilp} y_2}{m_{pile}} \tag{3.44}$$

$$\ddot{\theta} = \frac{F_h \mu_d sgn|y_2 - y_4 L_\beta \cos(\beta)| L_\beta cos(\beta) + F_{pre} L_\beta \sin(\beta) + m_{pad} g L_\beta cos(\beta)}{I_{triangle}}$$
$$\frac{-k_{cyl}(U_d - L_\alpha y_3) L_\alpha + c_{cyl} L_\alpha^2 y_4 - k_{eq} \theta L_\beta^2 sin(\beta)^2}{I_{triangle}} \tag{3.45}$$

The input of the solver is $\dot{y}(t, y)$ calculated with the initial values Equation 3.46 when the simulation starts or with the output values of the last time step of the stick solver when changing from stick to slip Equation 3.47. The solver's output is y(t). Every time step, the input values of the solver are calculated with the output of the previous time step.

$$y(t=0) = \begin{bmatrix} y_1(t=0) \\ y_2(t=0) \\ y_3(t=0) \\ y_4(t=0) \\ y_5(t=0) \end{bmatrix} = \begin{bmatrix} z_{pile}(t=0) \\ \dot{z}_{pile}(t=0) \\ \theta(t=0) \\ \dot{\theta}(t=0) \\ z_{lugre}(t=0) \end{bmatrix} \tag{3.46}$$

$$y(t=end_{slip}) = \begin{bmatrix} y_1(t=end_{stick}) \\ y_2(t=end_{stick}) \\ y_3(t=end_{stick}) \\ y_4(t=end_{stick}) \\ y_4(t=end_{stick}) \end{bmatrix} = \begin{bmatrix} z_{pile}(t=end_{stick}) \\ \dot{z}_{pile}(t=end_{stick}) \\ \theta(t=end_{stick}) \\ \dot{\theta}(t=end_{stick}) \\ z_{lugre}(t=end_{stick}) \end{bmatrix} \tag{3.47}$$

Slip-to-stick transition

When a transition from slip to stick happens, the relative velocity between the pile and pad changes direction. When the relative velocity changes from a positive to a negative value, the other way around or zero, the pile and pad will stick to each other again. In Equation 3.48, the relative velocity is calculated, whereas the velocity of the pad can be calculated as in Equation 3.48.

$$v_{rel} = \dot{z}_{pile} - \dot{z}_{pad} \tag{3.48}$$

$$\dot{z}_{pad} = \dot{\theta} L_\beta \cos(\beta) \tag{3.49}$$

When Equation 3.50 is true, the simulation must change from the slip solver to the stick solver. The signum of a function outputs the "direction" of a value, so +, -, or zero, and the relative velocity of the current time step needs to be compared with the relative velocity of the previous time step.

$$sgn(v_{rel_t}) \neq sgn(v_{rel_{t-1}}) \tag{3.50}$$

Solver Overview

Due to the difference in degrees of freedom in stick and slip, two different solvers must be used in Matlab. In stick, the system only has the degree of freedom of the pile since the motions of the pile and upper centralizer are related. Constraint equations can describe the relation between the motions of the pile and upper centralizer. See Equation 3.21. In slip, the pile and the upper centralizer have their own degree of freedom. Hence, the slip solver has more variables. The condition to change from stick to slip (Equation 3.32) and from slip to stick (Equation 3.50) determine whether the stick solver or the slip solver will be used. A schematic overview is made in the flowchart in Figure 3.5. To start the pile-driving, the pile must first reach its self-weight penetration. To reach this, a third solver is used without the interaction of the template.

In Matlab, the flowchart is run through every time step, checking if it is in the suitable solver or needs to stop the simulation and start the next solver. The model will begin at t = 0. A solver is started without a template. The pile will penetrate the soil until the self-weight penetration is reached. The self-weight penetration is reached when soil resistance is larger than the mass of the pile and hammer. When the self-weight penetration is reached, the pretension is applied to the pads, and the stick solver will start. After the first time step, the solver will check whether the condition to change to the slip solver is met. If it meets the condition, the slip solver will start the next time step and takes the last values of the stick solver as initial conditions. If the condition is not met, the simulation stays in stick. Precisely the same will happen for being in slip and changing to stick. The solver stops when the end time of the simulation is reached.

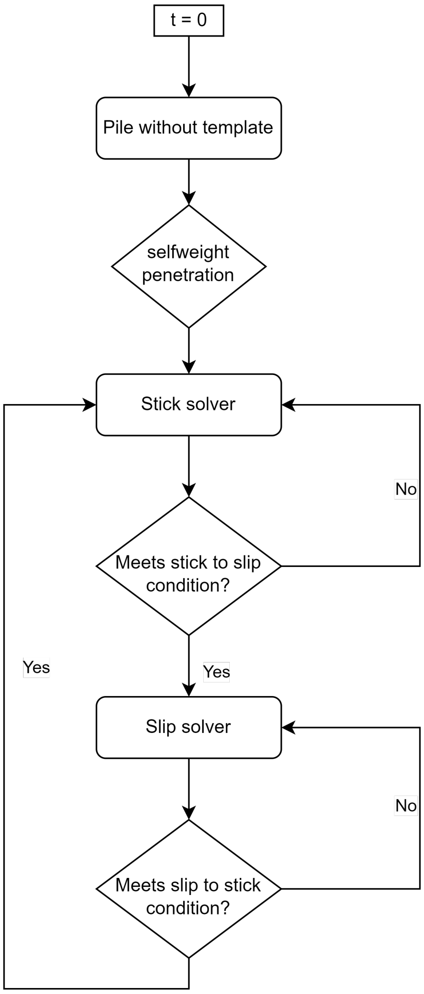

Figure 3.5: The flowchart of the model

4

Model Verification & Validation

This chapter presents the verification and validation of the model, which is crucial to interpret results and draw conclusions. If it is unclear to what extent this model resembles reality, the results of the model are useless. Verifying a model focuses on evaluating whether a model is designed and implemented correctly. The purpose of the verification is to identify and fix modeling errors. Validation of the model focuses on assessing the performance of the model, for example, by comparing its results with available data from measurements or literature. The model has different components and areas of attention, being the hammer force, the pile-soil interaction, the stick-slip solver system and the interaction between the pile and the template.

4.1. Validation of the soil-pile interaction

First, the interaction between the pile and the soil is validated. This validation is based on measured soil data collected in the preliminary stage of the development of the Changfang and Xidao wind parks by Boskalis. The resistance of the soil is measured with the use of cone penetration tests. These tests are subsequently used to calculate the expected behavior of the pile during pile driving. These calculations are done per location where a jacket needs to be installed. The exact place and spot used in this case are confidential. With the soil data obtained from the cone penetration tests, the expected self-weight penetration of the pile can be determined. The self-weight penetration of a foundation pile is the amount of penetration into the seabed due to its mass and the mass of the impact hammer. The pile will penetrate the seabed until the soil resistance is larger than the self-weight of the pile and hammer. The expected self-weight penetration overview is shown in Figure 4.1. The colored lines show the soil resistance to drive (SRD) for different scenarios. The best estimate SRD (red line) is used in this case. SRD is the force needed to drive the pile into the soil. The black line in Figure 4.1 is the self-weight of the pile and hammer. For the best estimate SRD, a self-weight penetration is expected at a penetration depth of 8 to 17.8 meters. The best estimate means that this soil resistance is considered the most likely value, which provides the most reliable approximation of the actual value. The expected self-weight penetration of the pile and hammer, using the best estimate SRD, is around 9.8 meters. The self-weight penetration range is extensive due to the different soil layers over depth. A constant soil layer is assumed for the model.

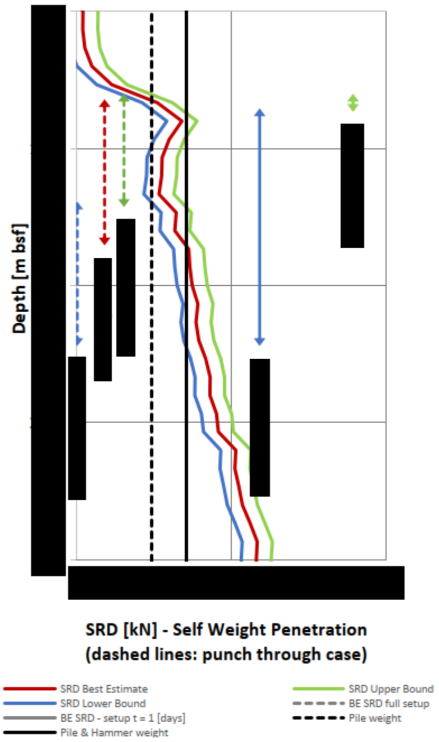

Figure 4.1: Estimated self-weight penetration of the pile [40]

In Figure 4.2, in blue, the pile penetration without the template in m as a function of time s can be seen. This penetration results from the model without interacting with the pre-piling template and applying six hammer blows. The mass of the hammer is taken into account. At t = 0 seconds, the pile is lowered into the soil. At t = 22 seconds, the pile reached its self-weight penetration at around 10 m. This self-weight penetration matches the expected self-weight penetration of the calculations from Figure 4.1.

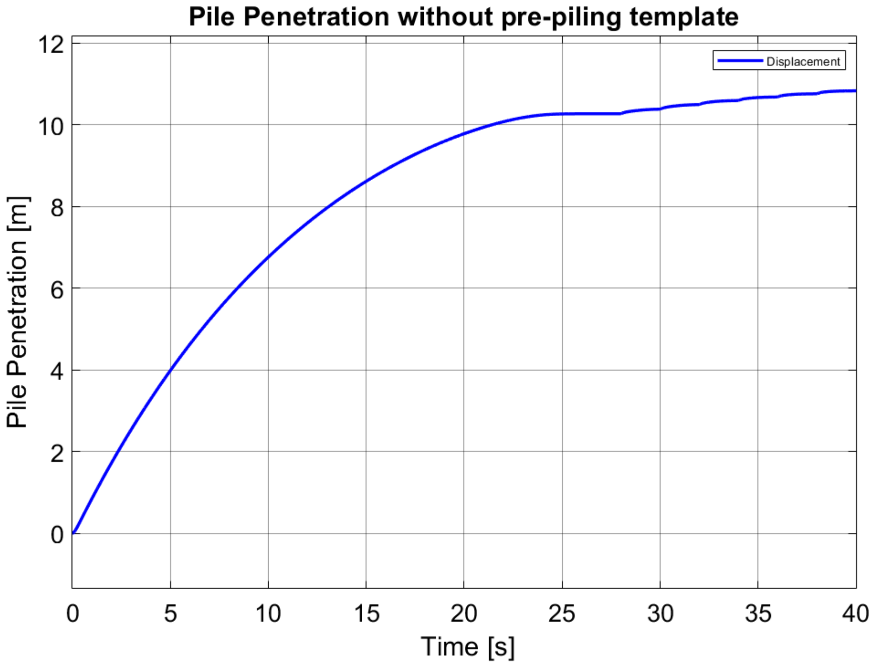

Figure 4.2: The pile penetration without template and with a hammer energy of 10% of the total capacity

Other calculations done by Boskalis based on the cone penetration tests are the number of blows needed to penetrate the soil 0.25 m. To drive the pile efficiently into the soil, the energy used by the impact hammer varies over depth. When the pile has a larger penetration depth, the soil resistance is larger, and the used hammer energy also needs to be larger to achieve the same penetration per blow of the hammer. The expected hammer energy over depth is given in Figure 4.3b. The depth is expressed in meters below the seafloor (m BSF). In the hammer model, the same input energy over depth is used. In Figure 4.3a, the expected number of hammer blows needed to gain 0.25 m penetration is given. The expected blows/0.25m around the self-penetration for all the soil conditions is around 3/4 blows. In Figure 4.4, the blue line represents the pile penetration without the template in m as a function of time s is shown from the self-weight penetration during six hammer blows. The blow count per 0.25m is around three blows, so this is of the same order. However, this comparison is inaccurate since the calculated data is challenging to read in Figure 4.3a.

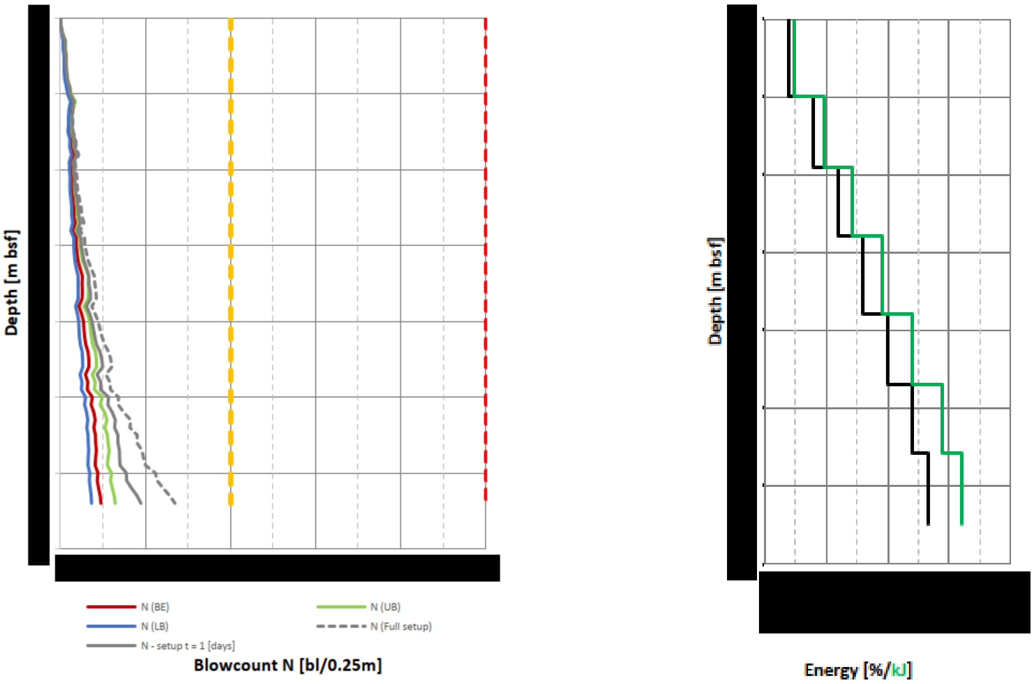

(a) Number of hammer blows needed to penetrate soil 0.25 meter [40]

(b) The expected hammer energy needed over depth [40].

Figure 4.3: Soil data provided by Boskalis, this soil data is gathered at one of the locations to install a jacket at the Changfang and Xidao wind farms [40].

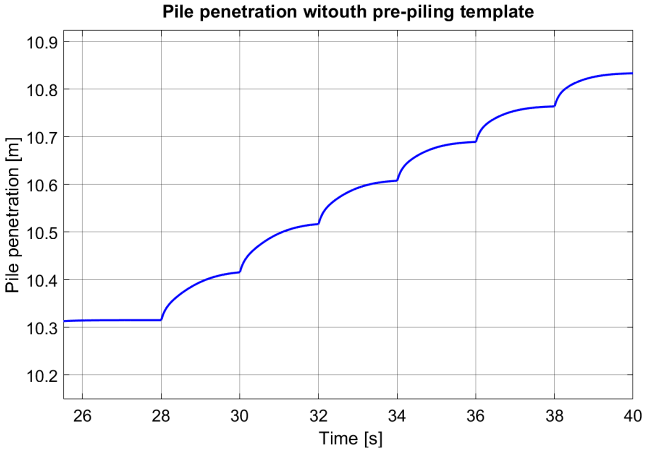

Figure 4.4: Close up of the pile penetration without template and with a hammer energy of 10% of the total capacity

Another way to verify the pile-soil model is to increase the input energy of the impact hammer. It is expected that the penetration of the pile will increase when the energy input increases as well. In Figure 4.5, the input force of the hammer onto the top of the pile can be seen. The energy used for this calculation varies between 10% and 100%. Since the hammer force is determined by the impact velocity Equation 3.8 and the impact velocity is determined by kinetic energy, double the amount of energy will result in $\sqrt{2}v_0$ and $\sqrt{2}F(t)$, see Equation 4.1 and Equation 3.8. The derivations of these ratios can be seen in Appendix D. $F(t)$ is the hammer force over time, E_{hammer} is the input energy of the hammer, and m_{ram} is the mass of the ram in the hammer. In Figure 4.5, the hammer force [N] as a function of time s for different hammer energy inputs can be seen. With double the amount of energy, the force is multiplied by $\sqrt{2}$. The pile penetration m as a function of time s with different hammer energy inputs can be seen in Figure 4.6. Six hammer blows were applied and the penetration is shown from the self-weight penetration during the six hammer blows. The penetration increase does not have the same ratio as the increase of the force since the resulting soil force is dependent on the velocity and displacement. However, the increase in energy between 25% to 50% and 50% to 100% leads to the same increment of the pile penetration between 25% to 50% and 50% to 100%, which is expected.

$$v_0 = \frac{2E_{hammer}}{m_{ram}} \tag{4.1}$$

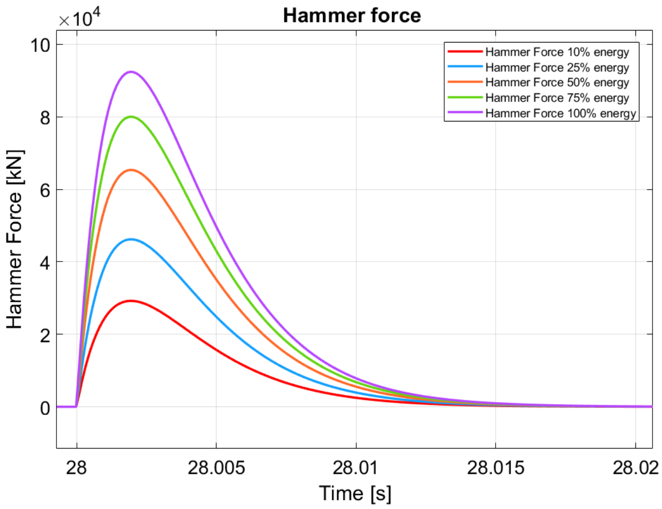

Figure 4.5: Pile penetration without template and hammer force using varying hammer energy

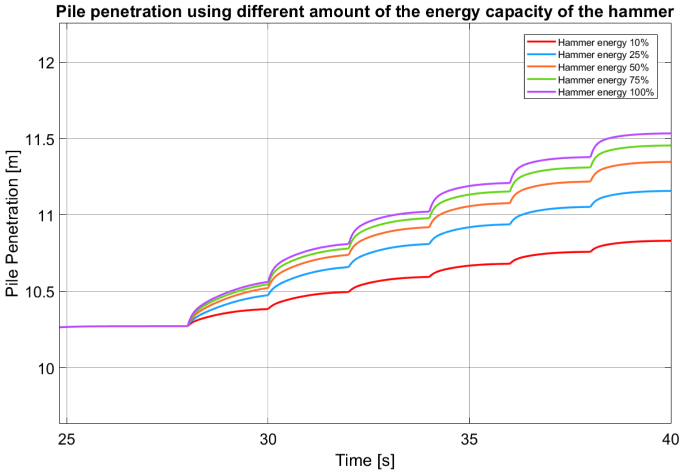

Figure 4.6: Pile penetration without template and with a varying hammer energy

4.2. Verification of the stick-slip interaction between pile and template

4.2.1. Varying the dynamic and static friction coefficient

This section will verify the interaction between the pile and the template. To test the interaction, the dynamic friction coefficient μ_d will be varied between 0 and 0.3 [-]. The pads' static friction coefficient μ_s is set at 0.3 [-] for this verification. The static friction coefficient of 0.3 is the by Huisman calculated static friction coefficient between the pile and friction pads. So only difference in behavior is expected during slip. In Figure 4.7, the pile penetration in m as a function of time in s applying two hammer blows can be seen. The different colors represent the pile penetration for different dynamic friction coefficients. The penetration is only shown during the two hammer blows. The pile penetrates the soil more per hammer blow when the dynamic friction coefficient is lower and the duration of the penetration is longer. This can be explained due to the lower dynamic friction force. The friction force slows down the pile less. In Figure 4.8, the rotation of the upper centralizer in rad as a function of time in s applying two blows can be seen. The lines in different colors represent the rotation of the centralizer for different dynamic friction coefficients. The rotation is only shown during the two hammer blows. The upper centralizer rotates less when the dynamic friction coefficient is lower. The duration of the slip period is also longer using a lower friction coefficient because the pile slows down slower. This behavior of both the pile and upper centralizer is expected.

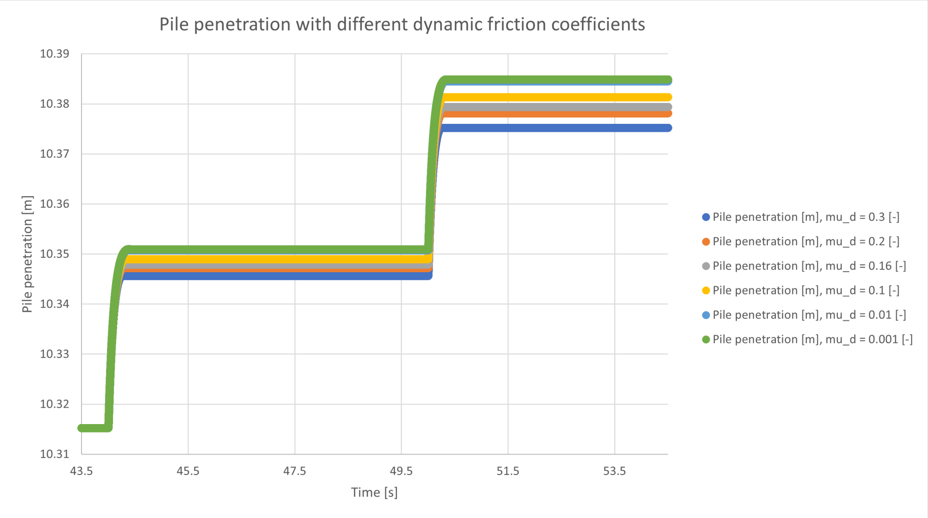

Figure 4.7: behavior of the pile with different μ_d

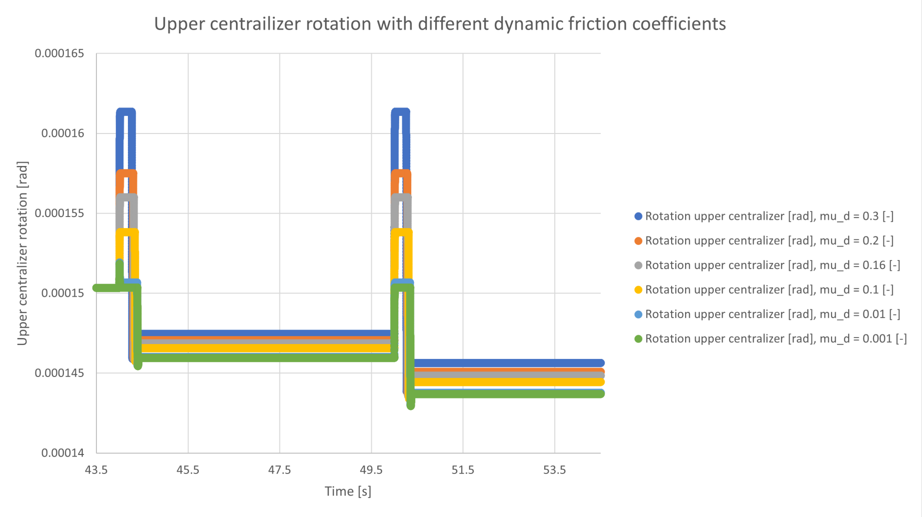

Figure 4.8: behavior of the upper centralizer with different μ_d

A simulation checks whether the combined model gives the expected results, where the static and dynamic friction coefficients μ_s and μ_d are set to zero. When the static friction coefficient is set to zero, no stick-slip switch is expected since the system is in constant slip because there is no interaction between the pile and pad. The pile penetration per blow is expected to be the same as in Figure 4.2. In Figure 4.9, in blue, the penetration in m as a function of time in s from the self-weight penetration applying two blows can be seen. The penetration per blow with a static friction force set to zero is the same as in the configuration without the template.

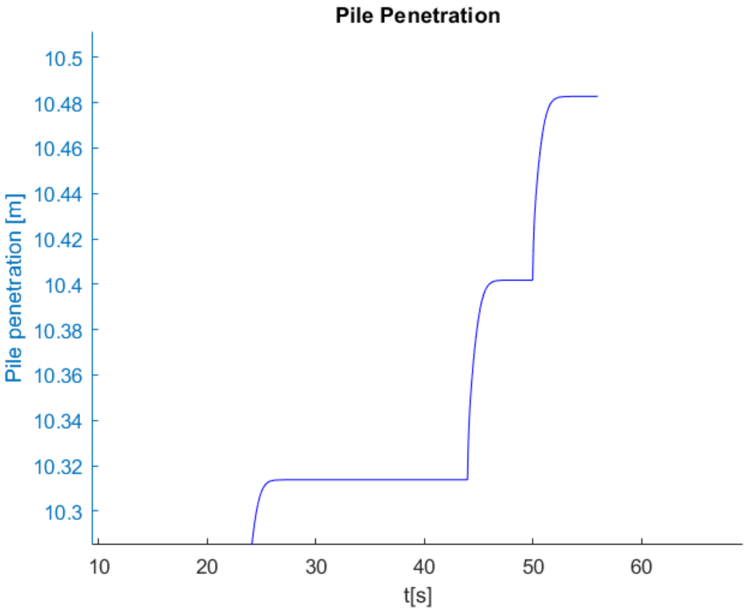

Figure 4.9: The static friction coefficient is set to zero to verify the pile penetration in the combined model

4.2.2. Verification of the relative velocity between the pile and pad

In Figure 4.10 to Figure 4.11b, the difference between the velocity of the pile and pad during two hammer blows can be seen. The blue line represents the velocity of the pad in m/s as a function of time in s and the red line represents the velocity of the pile in m/s as a function of time in s. The difference in velocity, which can be seen in these figures, is calculated during the simulation with two hammer blows. In Figure 4.11a, in the beginning, the velocity of the pile and the pad is the same. This is due to the stick period before the first hammer stroke. When the hammer force acts on the top of the pile, the pile begins to penetrate the soil. During stick, the pad moves with the same velocity as the pile. Then, the slip period begins and the upper centralizer slows down. When the pile slows down, the relative velocity becomes zero, the stick period starts, and again the pad moves with the same velocity as the pile. In Figure 4.11a, in a close-up of the first blow, the rough difference in velocity can be seen during slip. Because the separation of the pile and pad velocity is not very clear, vertical lines are added to show the moment the system is in stick or slip. In Figure 4.11b, a close-up of the first blow in Figure 4.10 is made. The close-up gives a detailed overview of the differences in velocity between the pile and pad during stick and slip.

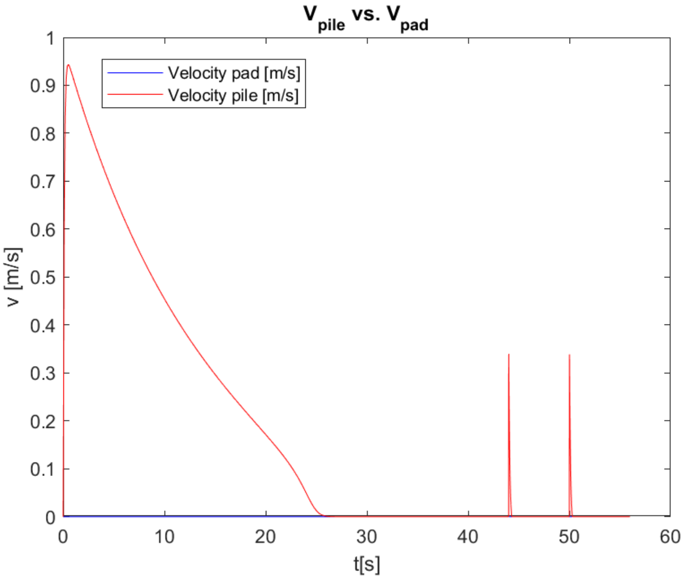

Figure 4.10: The velocity of the pile versus the velocity of the pad

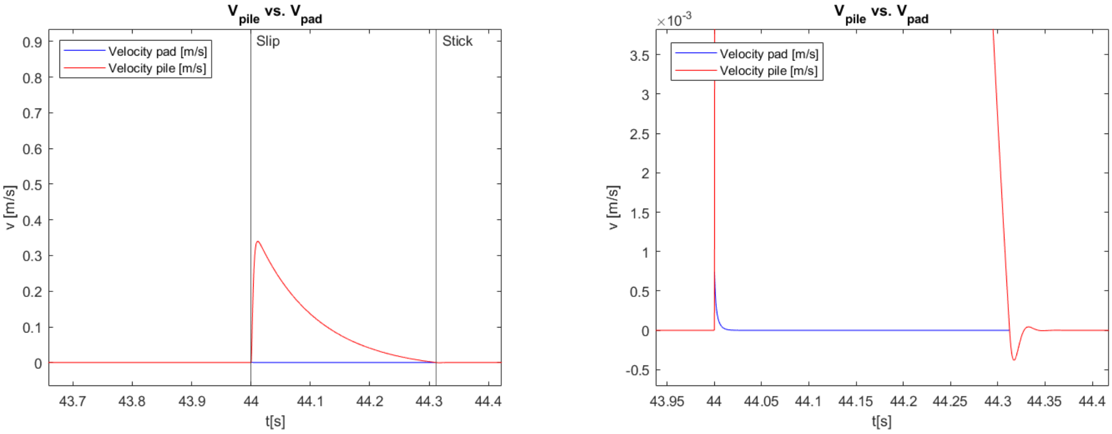

(a) A close-up of the relative velocity during the switch between stick and slip

(b) A close-up of the relative velocity during the switch between stick and slip

Figure 4.11: A close-up of the relative velocity during the switch between stick and slip

4.3. Validation of the model using measurements and literature data

4.3.1. Validation of the combined model using field data

Unfortunately, accurate validation of the combined model using field data was impossible. The available data gathered during the installation of Changfang and Xidao was measured at 1 Hz. Since the duration of a blow of the impact hammer is typically of the order of 10-20 milliseconds, a lot of valuable data wasn't measured. To capture the template's response accurately enough the sample rate should have been around 5 kHz to capture the template's response accurately enough. Another problem in capturing data during pile driving was the location of the accelerometers. The accelerometers were located at the center of the pre-piling template and not at the upper centralizers. Nothing could have been said about the behavior of the upper centralizers. However, vibration transferred from the pile to the template could have been seen. To validate the model in the future, data needs to be gathered at a frequency high enough to collect valuable information on the interaction between the pile and the pre-piling template. Also, the location of the sensors needs to be reconsidered.

4.3.2. Validation of the stick-slip solver

A simple mass-spring system on a conveyor belt validates the solver layout and the conditions when changing between stick and slip. The solvers used in this example are in the same configuration as in the complete model. The modeled system is schematically represented in Figure 4.12. The results are validated with a conveyor-belt example by Chen, S. & Zhang, Z. [41]. This paper compares a switching model only using static and dynamic friction coefficients, called Coulomb-stiction, and the use of the Stribeck effect. The Stribeck effect takes the change in dynamic friction force due to the change in velocity into account. Since the Stribeck effect is neglected for the pile and friction pads interaction, only a comparison is made with the Coulomb-stiction results. The same parameters as in the paper are used. The parameters can be seen in Figure 4.13. The The$v(t)$, a mass m, spring stiffness k, a static friction coefficient μ_s, and a dynamic friction coefficient μ_k. The mass first sticks to the belt and displaces at the same speed as the conveyor belt. The spring force, F_k, increases with the displacement. The static friction force is derived as Equation 4.3. When Equation 4.4 is met at 0.74 m, the mass will slip and be pulled back by the spring until the relative velocity between the mass and the belt is zero or changes direction.

$$F_k = u_1 k \tag{4.2}$$

$$F_{f,static} = \mu_s F_N, \text{ where } F_N = mg \tag{4.3}$$

$$F_k >= F_{f_static} \tag{4.4}$$

$$u_1 >= \frac{\mu_s F_N}{k} \tag{4.5}$$

$$u_1 >= 0.74m \tag{4.6}$$

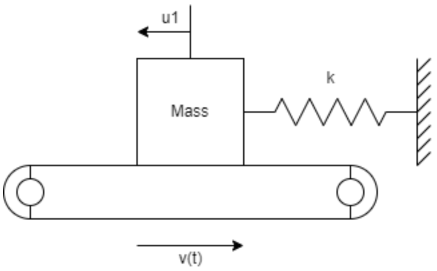

Figure 4.12: Simplified conveyor-belt system to prove the concept of stick-slip

Parameter	Value
mass of the body, m [kg]	1
belt velocity, $v(t)$ [m/s]	0.1
spring stiffness, k [N/m]	2
static friction coefficient, μ_s [-]	0.15
dynamic friction coefficient, μ_d [-]	0.1
initial velocity, v_0 [m/s]	0.1
gravity acceleration, g [m/s^2]	9.81

Figure 4.13: Parameters of the conveyor belt example

In Figure 4.14a, the displacement and velocity of the mass on the belt can be seen. The blue line represents the displacement of the mass in m on the conveyor belt as a function of time in s and the red line represents the velocity of the mass in m/s on the conveyor belt as a function of time in s. Both displacement and velocity can be read at the x-axis. This is the result of the switching model made in Matlab using the solver layout from Figure 3.5. Also, the relative velocity can be seen in Figure 4.14b. Here the red line represents the relative velocity between the mass and the conveyor belt as a function of time. The vertical black lines show the moment the model switches to stick or slip. The mass is transitioning from stick to slip at u1 = 0.74 m. Also, the mass sticks to the conveyor belt again when the relative velocity between the belt and mass is zero or changes direction. In Figure 4.15a and Figure 4.15b, respectively, the displacement in m and the velocity in m/s as a function of time of the mass calculated using [41] can be seen. The results are comparable, and the moments of transitioning between stick and slip happen at the exact moments at the same displacements.

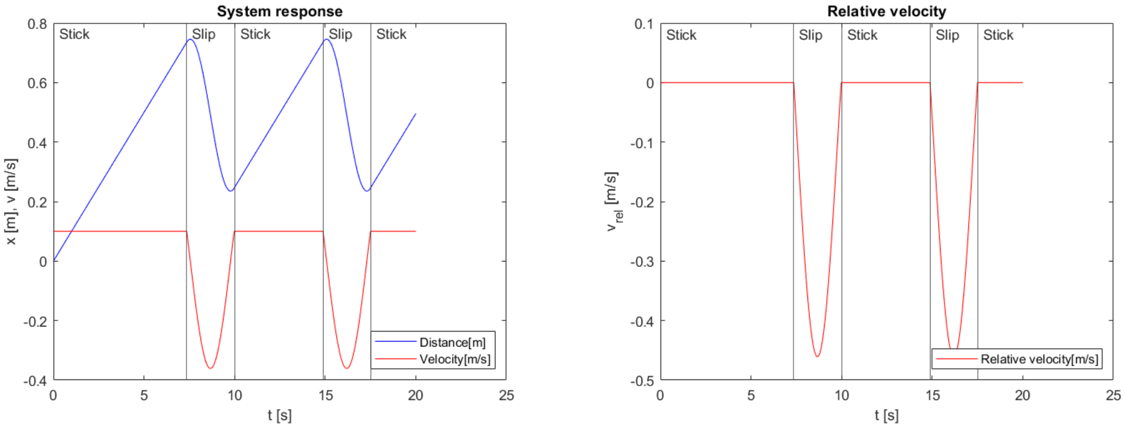

(a) The displacement and velocity of the mass on conveyor-belt.

(b) Relative velocity between the mass and conveyor-belt.

Figure 4.14: The results of the mass on the conveyor-belt using stick-slip switching model.

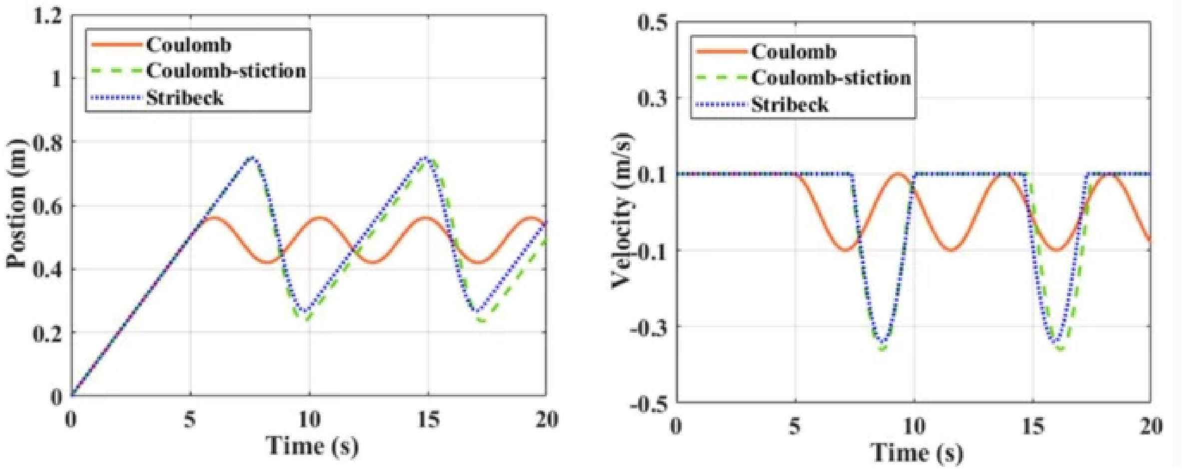

(a) The displacement and velocity of the mass on conveyor-belt [41].

(b) Velocity of the mass on the conveyor-belt [41].

Figure 4.15: The results of the mass on the conveyor-belt [41]

4.3.3. Validation of the impact hammer model

In this section, the hammer force over time is validated. The hammer force is applied on the top of the pile as an external force, using the analytical model proposed by Deeks & Randolph [33]. The BSP 357 hammer is used in the paper's analytical model. In Figure 4.16a, the force-time of the BSP 357 hammer can be seen. It is compared with field data of the same hammer. The thick black line shows the hammer force calculated by the model in the literature in kN as a function of time in s, the thin black line shows the hammer force from the field data in kN as a function of time in s. The peak force and the duration of the force are the same for the analytical model and the field data. However, the analytical force curve is much smoother since the hammer and pile vibrations are neglected in the analytical model.

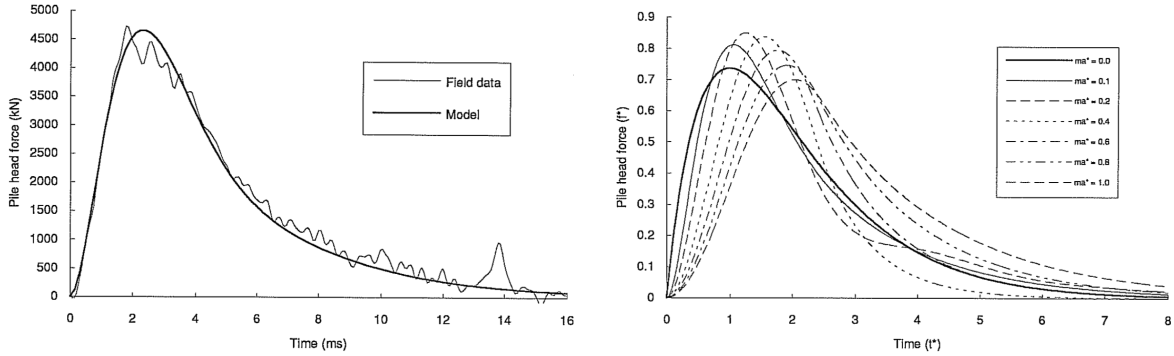

(a) Force-time curve of the BSP 357 Hammer validated with field data. [33]

(b) Comparison of the influence of different dimensionless anvil masses [33]

Figure 4.16: Force-time graphs of the BSP357 hammer, the left figure validated with field data and the right figure is the dimensionless force with different dimensionless anvil masses [33].

For the model in this thesis, a Menck 1900s hammer is used. The energy capacity for this hammer is 1900kJ. When the capacity of the hammer is ultimately used, a force-time graph is calculated, which can be seen in Figure 4.17. The blue line represents the hammer force in N as a function of time in s. The dimensionless force-time graph of the Menck hammer can be seen in Figure 4.18. The blue line represents the dimensionless hammer force as a function of dimensionless time. Since the mass of the anvil of the Menck hammer is unknown, it is assumed to be zero in the analytical model. A comparison can be made with Figure 4.16b. In this figure, the dimensionless force over time, the different black lines represent different dimensionless hammer force curves for different dimensionless anvil masses. Due to the neglected anvil mass, the force will increase faster than with anvil mass. However, this only influences the peak force. The transferred energy will be roughly the same. It is hard to compare the force-time graph of Figure 4.17 with Figure 4.16a. The energy capacity for the BSP 357 hammer is unknown, so it is hard to compare the peak force of the Menck and the BSP 357 hammer. Also, different ram masses and piles are used. The only comparison can be made between the shape of the dimensionless force of the BSP 357 hammer and the Menck 1900s hammer. An anvil mass is used for the BSP 357 hammer. For the Menck hammer, the anvil mass is neglected. So, there is an expected difference in the start of the force-time graph of the BSP and the Menck hammer.

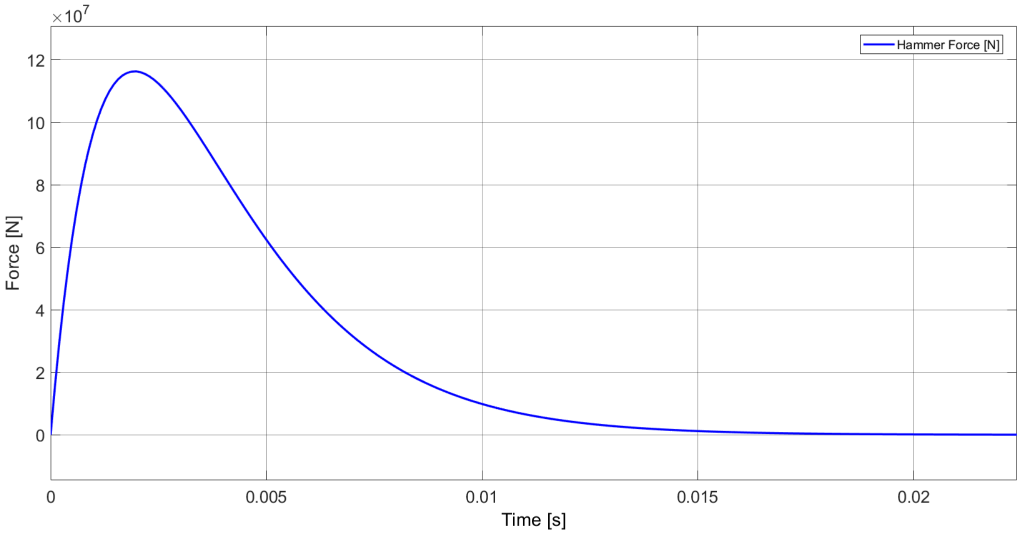

Figure 4.17: Force-time curve of the Menck 1900s hammer calculated using the hammer model.

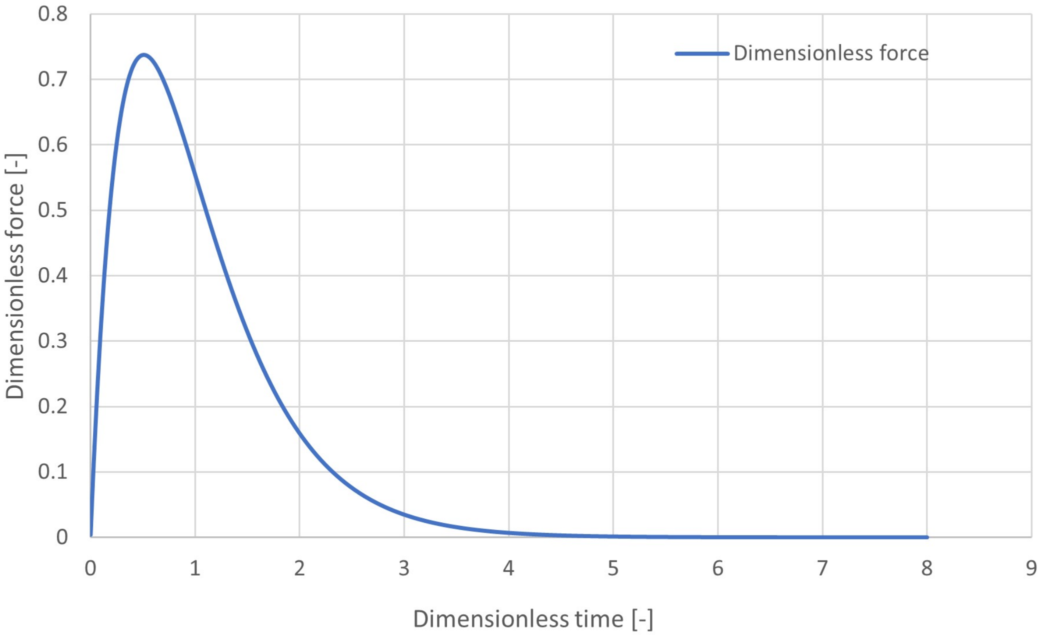

Figure 4.18: Dimensionless force-time curve of the Menck 1900s hammer calculated using the hammer model.

4.4. Discussion

First, the pile-driving was verified without interacting with the pre-piling template using collected soil data from the installation locations. The expected self-weight penetration of the pile corresponds with the results from the model. Also, the penetration per hammer blow does correspond to the expected penetration. Soil can vary a lot over the area of an installation location, and a soil profile over the depth is never homogeneous. In this model, the soil parameters are the same for the whole depth and area of the location. The resistance of the soil increases linearly with the depth. The results of the pile-soil interaction will be an interpretation of reality and will never give the exact results. Finally, the increase of the penetration due to the increase of hammer force was related to each other, and no unexpected results were seen.

The interaction between the pile and the upper centralizer during slip, alternating the dynamic friction coefficient, meets the expectations. The pile penetrates the soil more, and the upper centralizer rotates less when lowering the dynamic friction coefficient. When the static friction coefficient is set to zero, the behavior of the pile is the same as the behavior of the pile without a pre-piling template.

The difference in velocity between the pile and the pad is acting as expected. The velocities are equal during stick, and the pad and the pile have different velocities during slip. The system changes to stick when the relative velocity becomes zero.

After that, the use of the different alternating solvers was validated using a simple model of a mass-spring system on a conveyor belt. Using results from a paper, switching between the stick and slip solver happened at the right time and displacement. Also, switching back from slip to stick happened when the relative velocity was zero. The solver layout has proven to work.

Finally, the model describing the impact hammer was validated using Literature data. Comparing this data, the dimensionless force-time curve of the Menck 1900s hammer does match the literature, which results in the curve in Figure 4.17. The analytical model is validated using field data from the BSP 357 hammer. However, the lack of field data of the Menck 1900S hammer makes it hard to predict exactly the force-time curve exerted on the top of the pile.

The different parts of the model are verified and validated. However, validating the combined model using experimental field data is impossible. The conclusions can be drawn qualitatively but not quantitatively. More field data is needed to validate the model quantitatively.

5

Results and analysis of the results

In this chapter, the results of the model and simulation are presented. Since the combined model isn't validated, the simulation results cannot be related to reality. However, the results will be analyzed, and conclusions will be drawn.

The simulations are done using the friction coefficients of the pad. The pad's static friction coefficient μ_s is 0.3 [-], and the dynamic friction coefficient μ_d is 0.16 [-]. The time step chosen for the simulation is $1 * 10^{-4}$ [s]. This time step is determined to collect enough data points during the impact of the hammer. Another critical parameter of the simulation is the pretension applied by the pads on the pile. The pretension applied on the pile is 98 kN. The initial values and the parameters can be found in Table 5.1. The impact hammer energy used is 10% following Figure 4.3b. First, a simulation is done with two hammer blows. Later a simulation applies six hammer blows.

Parameter	**Value**
Time step, Δt [s]	$1 * 10^{-4}$
Static friction coefficient, μ_s [-]	0.3
Dynamic friction coefficient, μ_d [-]	0.16
Pretension, F_{pre} [kN]	98
Initial penetration pile, z_{pile} [m]	0
Initial velocity pile, v [m/s]	0
Initial rotation upper centralizer, θ [rad]	0
Initial rotation upper centralizer, $\dot{\theta}$ [rad/s]	0

Table 5.1: Parameters for the simulation of the interaction between the pile and the pre-piling template

5.1. Response of the pile

In Figure 5.1a, the response of the pile applying two hammer blows can be seen. The blue line represents the pile penetration in m, see left x-axis, as a function of time in m and the red line represents the pile velocity in m/s, see right x-axis, as a function of time. In Figure 5.1b, a close-up of Figure 5.1a is made. First, the pile penetrates the soil until the self-weight penetration is reached. Until the self-weight penetration is reached, the pre-piling template isn't clamping and centering the foundation pile. At t=39 s, the pretension is applied to the pads, and the pads rotate and clamp the pile, see Figure 5.2a. In Figure 5.6, the normal force between the pile and pad at t = 39 s is 98 kN due to the pretension.

After the pretension is applied, the first blow is exerted on the top of the pile at t = 44 s. In both Figure 5.1a and Figure 5.1b, the penetration due to the blows of the hammer can be seen. Due to the static and dynamic friction force, the penetration of the pile is less than not clamped in by the pads of the pre-piling template. Where the penetration of the pile without the pre-piling template with the same hammer energy at the same soil depth was 8 cm (Figure 4.2). With the pre-piling template, the penetration of the pile is 4 cm per blow.

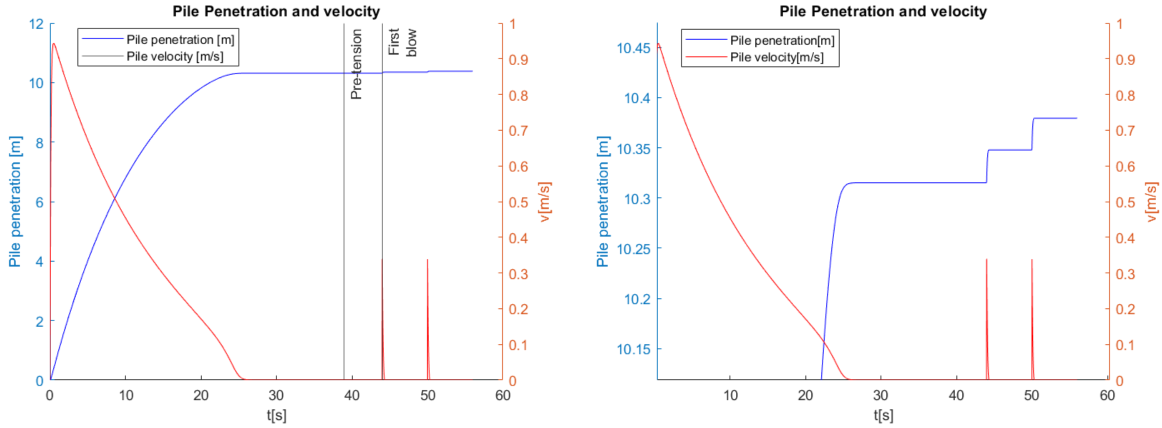

(a) Displacement and velocity of the pile with the template, $\mu_d = 0.16$ and $\mu_s = 0.3$

(b) Close-up of the displacement and velocity of the pile with the template, $\mu_d = 0.16$ and $\mu_s = 0.3$

Figure 5.1: Displacement and velocity of the pile with the template, $\mu_d = 0.16$ and $\mu_s = 0.3$

5.2. Template response during pile installation

In Figure 5.2a to Figure 5.3, the blue line represents the rotation of the centralizer in rad as a function of time in s during two hammer blows. In Figure 5.2a and Figure 5.2b, the black vertical lines represent the moment the pretension is applied and the moment the first hammer blow is applied. In Figure 5.3, the vertical black lines represent the moment the system is in stick or slip. First, the pads are disconnected from the pile. The rotation of the upper centralizer is zero, and there isn't any interaction between the pile and the pre-piling template. The pretension is applied on the pads when the pile reaches its self-weight penetration. The centralizer rotates at t = 39 s due to the applied pretension. After the pretension is applied, the first hammer blow is applied on the top of the pile. This happens at t = 44 s.

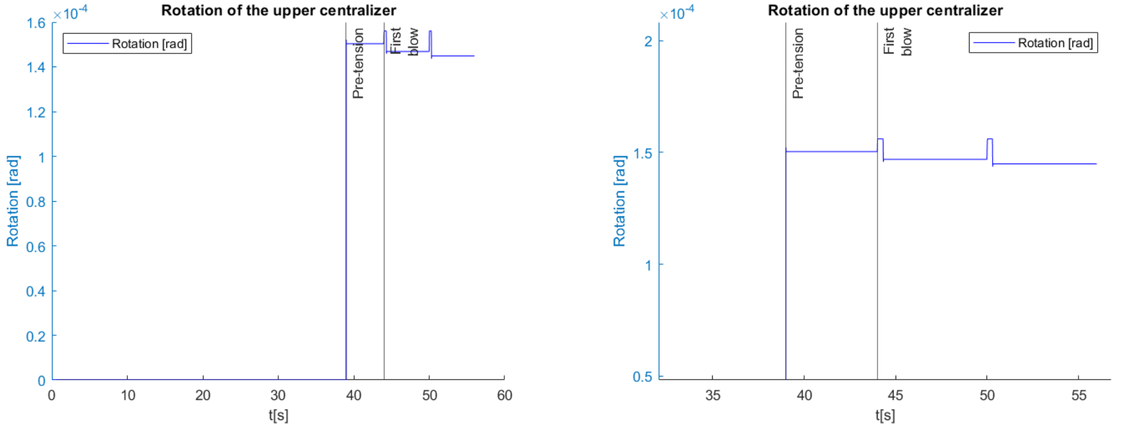

(a) Rotation of the upper centralizer of the template, $\mu_d = 0.16$ and $\mu_s = 0.3$

(b) Close-up of the rotation of the upper centralizer of the template, $\mu_d = 0.16$ and $\mu_s = 0.3$

Figure 5.2: Rotation of the upper centralizer of the template, $\mu_d = 0.16$ and $\mu_s = 0.3$

In Figure 5.3, a close-up is made at the time of the first blow. The upper centralizer rotates due to the hammer blow and because it sticks to the pile. Slip is initiated when the vertical force between the pile and pad is higher than the critical friction force. During slip, the rotation of the upper centralizer remains constant. The normal force remains constant, and thus also the friction force that rotates the upper centralizer in the positive direction. During slip, the moments around point C are balanced at this rotation. The upper centralizer's rotation depends on the dynamic friction coefficient, as seen in Figure 4.8. When the relative velocity between the pad and the pile becomes zero or changes direction, the pad and pile will stick again. At approximately t = 44.3 s, the relative velocity between the pile and pad is zero, so the pad and the pile will stick together. See Equation 3.48. However, due to the combination of the soil parameters and the damping in the system, the system is slightly underdamped. This causes the pile velocity to oscillate around zero before it comes to a stop. In Figure 4.11b, the oscillation of the pile can be seen. This results in a slight upward movement of the pile, and the upper centralizer rotates beyond the initial rotation due to the pretension.

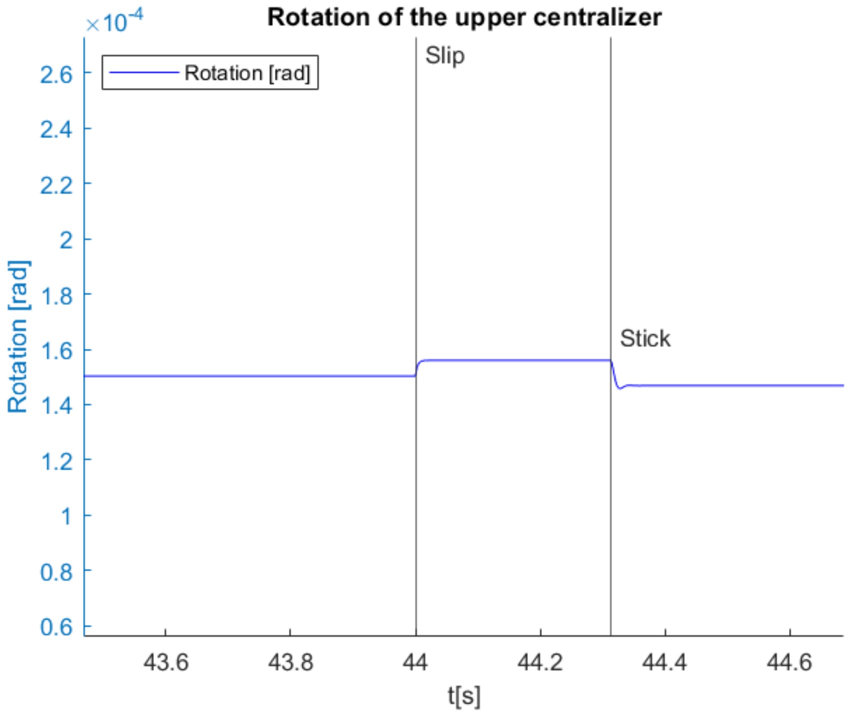

Figure 5.3: Close-up of the rotation of the upper centralizer of the template, $\mu_d = 0.16$ and $\mu_s = 0.3$

A simulation is done with six blows to see the upper centralizer's behavior after more than two hammer strokes. After three blows, a pattern emerged. This can be seen in Figure 5.4. The blue line represents the rotation of the upper centralizer in rad as a function of time in s. Due to the negative rotation after the first two blows, the normal force between the pile and pad has become less. Due to the lower normal force, the static friction force is also less. This results in more penetration and pile velocity during the third blow. The behavior during the third hammer blow is shown in the close-up of the centralizer rotation. First, the upper centralizer rotates until the equilibrium situation is reached, just as during the first two hammer strokes. When the pile stops, stick occurs. However, other than during the first two blows, the pile had a higher velocity and penetration, so it bounces back a bit more. This pile behavior results in another slip situation. This time, the friction force creates a negative moment on the centralizer. The relative velocity again becomes zero, and stick happens again. In Figure 5.5, a close-up of Figure 5.4 during the third hammer blow is made. Here, switching between stick and slip and the behavior of the upper centralizer during the third hammer stroke can be seen.

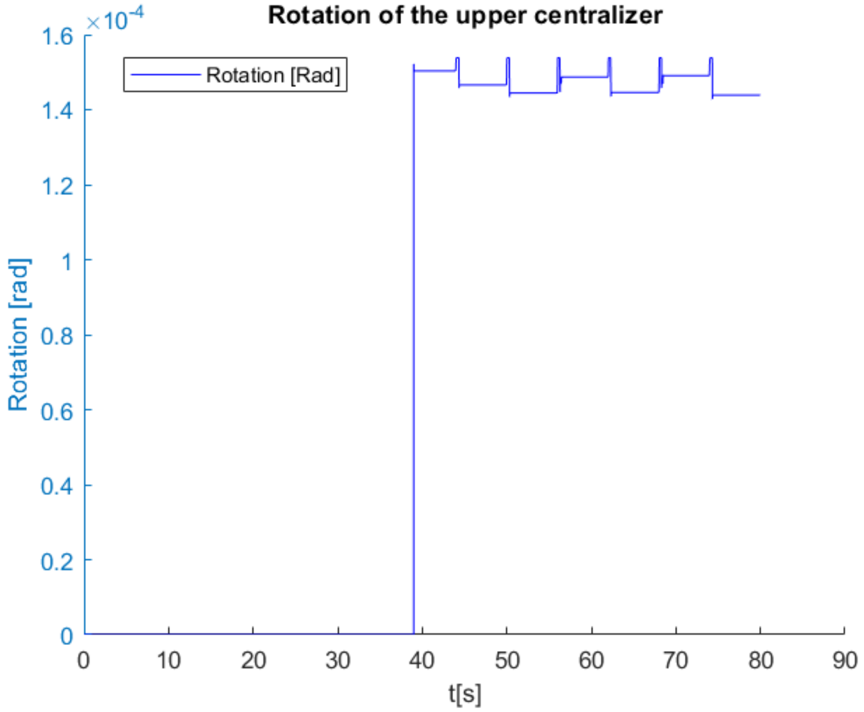

Figure 5.4: The rotation of the upper centralizer with six hammer blows, $\mu_d = 0.16$ and $\mu_s = 0.3$

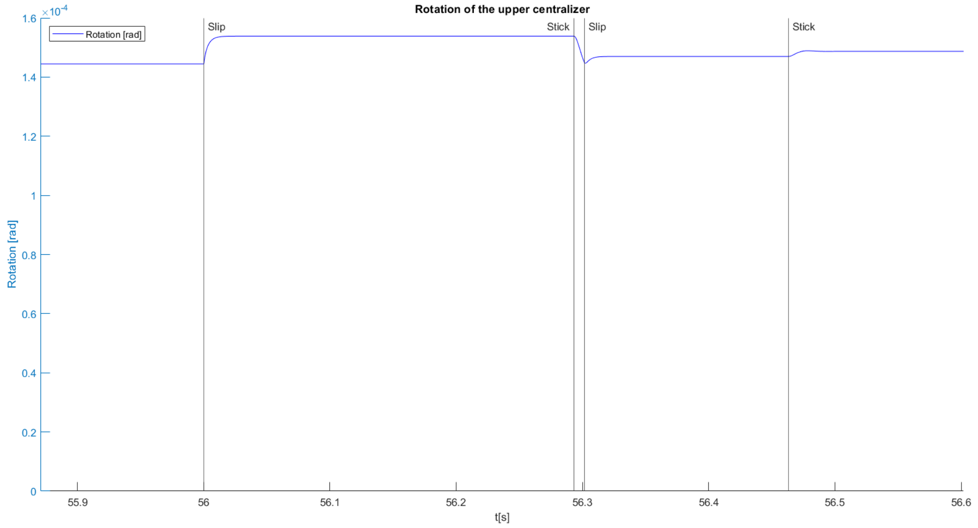

Figure 5.5: Close-up of the rotation of the upper centralizer with six hammer blows, $\mu_d = 0.16$ and $\mu_s = 0.3$

5.2.1. The normal force between the pile and pad

The normal force between the pile and pad is directly related to the rotation of the upper centralizer. In Figure 5.6, an increase in normal force can be seen during the slip periods of the simulation, two hammer blows where applied. The blue line represents the normal force in kN between the pile and pad as a function of time in s. The design of the upper centralizers causes the normal force to increase during pile driving. This results in a higher friction force between the pile and pad during slip. The pile penetrates the soil less per hammer stroke, and the upper centralizer rotates more.

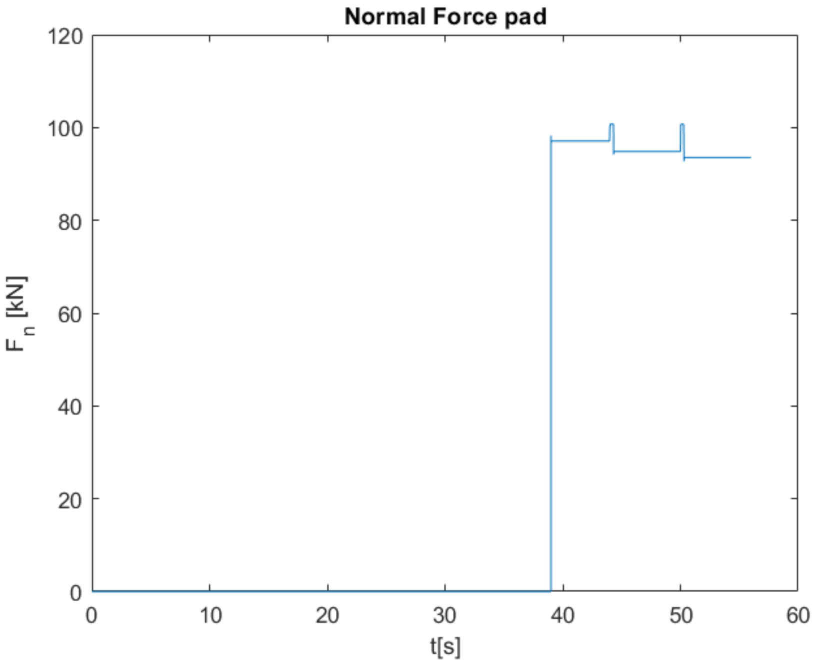

Figure 5.6: The normal force between the pile and pad

5.2.2. Comparison between roller and pad simulation

In Figure 5.7 and Figure 5.8, a comparison can be made between the simulation results of the pre-piling template with use of friction pads and the use of rollers applying two hammer blows. In Figure 5.7, the blue line represents the pile penetration with the use of rollers in m as a function of time in s and the orange line represents the pile penetration using friction pads in m as a function of time s. The figure shows the pile penetration due to two blows from the self-weight penetration. In Figure 5.8, the blue line represents the rotation of the centralizer with the use of rollers in rad as a function of time in s and the orange line represents the rotation of the centralizer using friction pads in rad as a function of time s. The figure shows the rotation due to two blows, the initial rotation is initiated by the applied pretension. In the simulation with friction pads, the static and dynamic friction coefficients are respectively 0.3 and 0.16. In the simulation to represent rollers, the static friction coefficient is set to zero, and the dynamic friction force is set very low. Modeling a roller means no stick since a roller is free to rotate. The low dynamic friction coefficient represents the rolling friction of a roller. In Figure 5.7, the penetration of the pile can be seen for both the configuration of the pads and the roller. There is a significant difference in penetration per hammer stroke. The penetration of the pile with a roller is much higher than with pads. Three blows are needed with the pads to gain the same penetration as using the rollers. In Figure 5.8, in the configuration of the pads, the upper centralizer moves just after the impact for the hammer. The energy lost in the penetration of the pile is converted into the rotation of the upper centralizers of the pre-piling template. The rotation of the upper centralizer in the simulation with rollers is constant due to the low friction force. The pretension initiates the initial rotation of the upper centralizer with rollers.

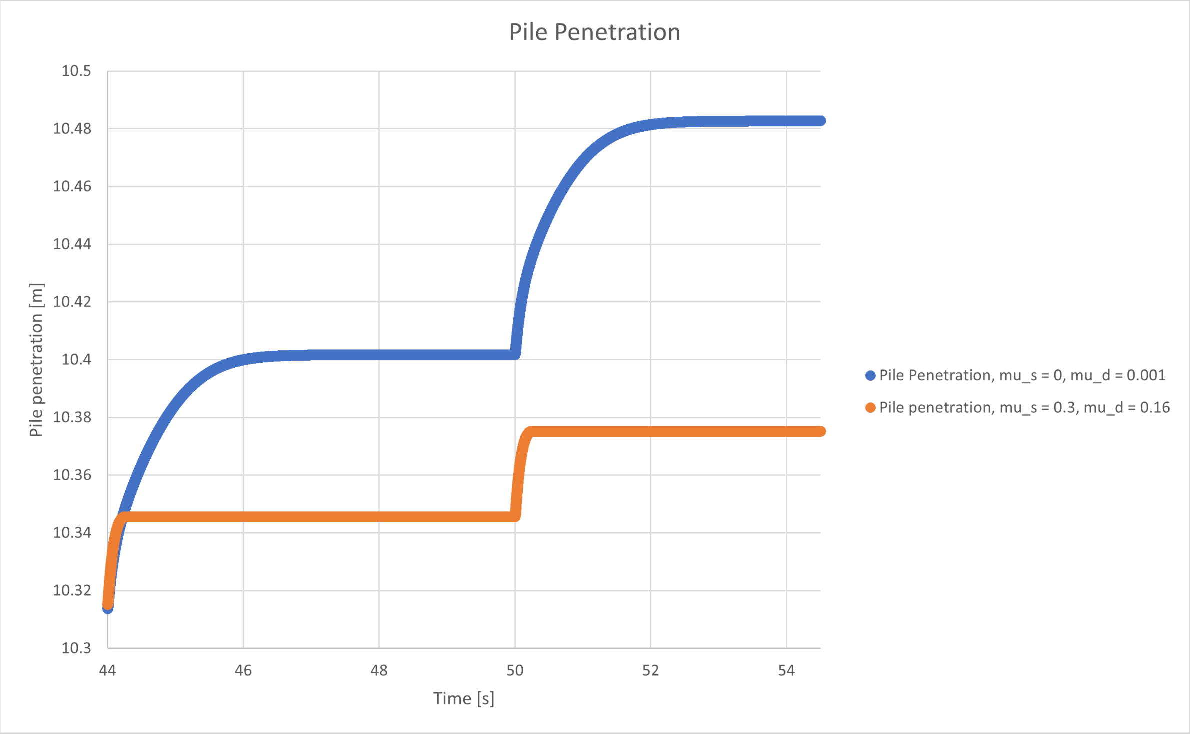

Figure 5.7: Results of the simulation to compare roller vs. pad, pile penetration.

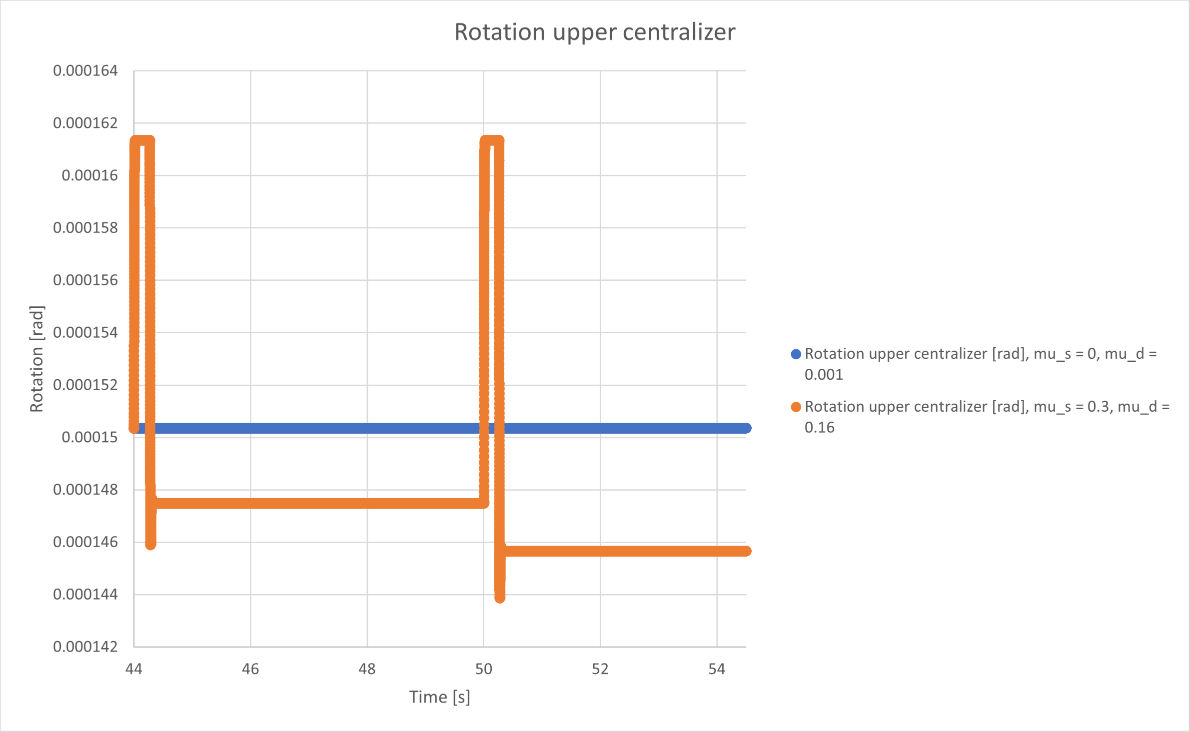

Figure 5.8: Results of the simulation to compare the rotation of the upper centralizer using rollers and pads.

To determine the energy dissipation due to the interaction of the pile with the pads during pile installation, a comparison is made between the power transferred by the pile and the power transferred by the pile to the pads. The difference between the powers determined gives the rate of the energy dissipation per hammer blow into the template. Power, P in watts, is the amount of energy transferred in a unit of time. The power is defined using work W and time t. Since work, W is defined as force F times displacement d and velocity v as displacement over time. Substituting Equation 5.2 into Equation 5.1 gives Equation 5.3. So by integrating the difference over time, the total energy dissipation, $E_{dissipated}$ in J per hammer blow can be determined.

$$P = \frac{W}{t} \tag{5.1}$$

$$W = F * d, \text{ where } v = \frac{d}{t} \tag{5.2}$$

$$P = F * v \tag{5.3}$$

The relative velocity of the pad $v_{relative,pad}$ with respect to the template and the vertical force F_v between the pile and pad is used to calculate the energy transferred from the pile to the pad. The relative velocity of the pad is equal to the velocity of the pad because the motions of the template are assumed zero. The vertical force is derived in Equation 3.22. Using Equation 5.4, the total energy dissipation into the template can be calculated. Comparing this to the applied energy by the hammer onto the pile gives us the percentage of energy loss per hammer blow.

$$E_{dissipated} = \int F_v * v_{relative,pad} * dt \tag{5.4}$$

With Equation 5.4, the total energy dissipated into all four upper centralizers can be calculated. In this simulation, the hammer's applied energy is 190 kJ, 10% of its maximum capacity. The total energy loss is 37 kJ or 19.5% of the applied energy per blow. Leading to less penetration depth of the pile, rotation of the upper centralizer and vibrations of the template. The calculated energy dissipation has a broad frequency spectrum and therefore, a significant amount of energy goes into high-frequency vibrations. These high-frequency vibrations can induce vibrations in the secondary steel. Resonance and fatigue can eventually cause damage to the template depending on the number of load cycles and the natural frequency of the secondary steel.

5.3. Discussion

The results show the behavior of the pile and pre-piling template during pile driving. The pile's behavior compared to the simulation results without the pre-piling template are quite different. An influence of the friction pads on the penetration of the pile can be seen in the decrease of pile penetration per hammer blow. This behavior is expected due to the additional friction forces acting on the pile.

The results of the simulation show that during pile driving, the upper centralizer rotates and increases the normal force between the pile and the pad. The rotation is started during stick. The pad first follows the pile, and when the resulting vertical force between the pad and the pile is larger than the friction force, slip is started, and the pad slows down. The pad doesn't rotate back to its initial position. This is due to the dynamic friction between the pile and the pad. This friction acts on the pad until the relative velocity between the pile and pad is zero or changes direction. Due to the upper centralizer's design and the triangle's point of rotation, the pads are pushed inwards as the pads move downward. Due to the friction between the pile and the pads, these pads move down with the pile during installation as long as the pads stick to the pile. The inward displacement of the pad increases the normal force. This leads to a larger friction force between the pile and the pad, which causes a decrease in pile penetration per hammer stroke and increases energy dissipation into the template.

In Figure 5.9, it can be seen that the pad moves inward and downward due to the upper centralizer's rotation. The initial position of the upper centralizer can be seen in black and the red upper centralizer represents the by θ rotated upper centralizer.

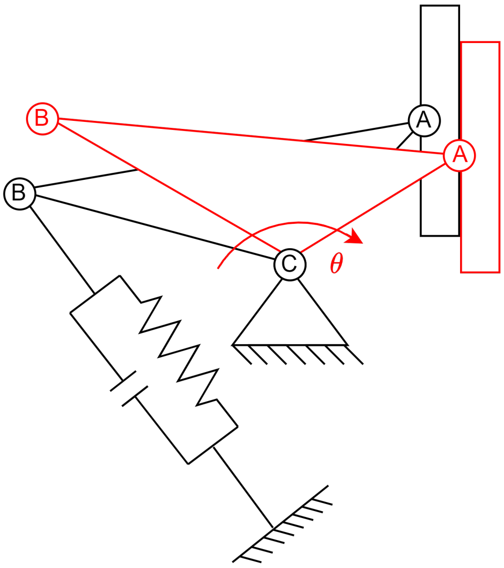

Figure 5.9: The rotation of the upper centralizer leads to an inward and downward displacement of the pad. The initial position of the upper centralizer can be seen in black and the red upper centralizer represents the by θ rotated upper centralizer.

When the pile is hammered down, before it stops moving, the velocity oscillates a bit around zero. The combination of soil parameters and damping in the system leads to a slightly underdamped system. The oscillation is not significant in relation to the penetration per blow and the velocity of the pile. However, it does lead to a new steady state position of the pad in stick.

The differences due to the changes in friction coefficient are expected. Due to a lower dynamic friction coefficient and a static friction coefficient of zero, the pile penetration is larger per hammer blow, and there is just a small rotation of the upper centralizer due to a minimal dynamic friction force. These results could be related to using a roller instead of pads. With the implementation of a roller, there is no stick and slip. The roller can move freely. This results in a penetration per blow comparable to that without the template and larger than using friction pads. The lower penetration per blow increases the number of blows for the complete pile driving process of the foundation pile. The template will be more often exposed to loads between the pile and the pad and energy dissipation into the template. The calculated energy dissipation has a broad frequency spectrum and therefore, a significant amount of energy goes into high-frequency vibrations. These vibrations cause the secondary steel to vibrate, which can damage this secondary steel.

From these results, conclusions can be drawn. However, these conclusions must be drawn carefully since the combined model is not validated.

6

Conclusion and Recommendations

6.1. Conclusions

This thesis examines the interaction between a foundation pile and a pre-piling template. A model was developed to describe the behavior of the pile and pre-piling template. The main objective was to identify the possible reasons for the damage to the pre-piling template's secondary steel. To complete the objective, a research question was stated:

What are the possible reasons for the damage to the secondary steel of the pre-piling template during the installation of the foundation piles?

This question is broken down into three sub-questions. These questions will be answered in this conclusion. Before answering the questions, it needs to be stated that the simulation results of the interaction between the pile and pre-piling template aren't validated by experimental or field data. The results and conclusions need to be quantitatively validated in future research.

1. What possible reasons could result in the pile template interaction causing damage to the pre-piling template?

To answer this sub-question, a literature review was performed. Based on the literature, there could be a few possible reasons causing additional loads on the template. Different loads described in the literature can cause potential damage to the template. First, there are hydrodynamic loads that can cause the piles to sway and apply extra loads on the template. Also, vibrations and radial expansion of the pile due to propagating stress waves through the pile due to pile driving can cause increasing loads and vibrations transferred from the pile to the template. Lastly, retrieving the template from the seabed and transitioning the template through the wave zone can also increase the loads on the template. The difference between the templates used in the literature and the template researched in this thesis is the use of friction pads instead of rollers. These friction pads could significantly influence the loads on the template.

2. How does the current design influence the interaction between the pile and the pad?

Due to the upper centralizer's design and the triangle's point of rotation, the pads are pushed inwards as the pads move downward. Due to the friction between the pile and the pads, these pads move down with the pile during installation as long as the pads stick to the pile. However, as explained, even during slip, the pads remain at a location lower than the original pad location. As a result, both during stick and slip, the rotation of the triangle in the upper centralizer causes the normal force between the pad and the pile to increase. This leads to even higher friction forces and therefore an even larger energy dissipation due to the pile-template interaction.

3. How can the design be adjusted so that less damage occurs to the pre-piling template?

Since many pre-piling templates use rollers instead of friction pads to centralize and align foundation piles, the choice was made to run some simulations with different dynamic and static friction coefficients. From the results using different friction coefficients, it could be concluded that using pads instead of rollers influences the pile's behavior and the pre-piling template. The pile penetration was less, and the rotation of the upper centralizer was more, using a higher friction coefficient. When the static friction coefficient was set to zero and only applied a very low dynamic friction force to the pile and pad, the pile penetration per blow was comparable to the pile without the template. The energy applied to the system was the same during both simulations. The results show more energy dissipation from the pile to the pre-piling template when using friction pads. The lower penetration per blow and the higher energy dissipation into the system lead to an increasing number of total blows during the complete installation of a foundation pile and, therefore, more load cycles. An increasing number of load cycles will faster lead to fatigue of the template. Using a low dynamic and no static friction coefficient can be seen as simulating rollers. Using rollers instead of friction pads will decrease the energy dissipation into the template. It would be plausible that less energy dissipation leads to less damage to the pre-piling template. A different orientation of the upper centralizer could also lead to a different interaction between the pile and the template. However, since the effect of different orientations isn't investigated in this thesis, further research is necessary to draw conclusions.

Coming back to the main research question:

What are the possible reasons for the damage to the secondary steel of the pre-piling template during the installation of the foundation piles?

It can be concluded that the use of friction pads and the orientation of the upper centralizer certainly influence the interaction between the pile and the pad. The design of this pre-piling template could be one of the possible reasons causing the damage to the template. Even though the results of the model have not been quantitatively validated, the model qualitatively shows that the use of friction pads causes a significant amount of pile driving energy to be transferred to the template. This not only leads to less energy being used for the pile penetration, thereby requiring additional blows and a longer installation time to reach the required penetration depth, but it also likely leads to the high-frequency vibrations that cause damage to the secondary steel of the pre-piling template. This effect is even amplified by the additional blows required to reach the required pile penetration.

Based on the results and conclusions, the hypothesis can be answered. Repeating the hypothesis:

The current design of the upper centralizers causes an increase of the peak normal force and thus of the friction force between the pile and pads while hammering the pile through the pre-piling template resulting in damage to the secondary steel of the pre-piling template.

Based on the conclusions, the hypothesis cannot be proven fully. The results do show an increased peak normal force between the pile and the pad, leading to an increased friction force between the pile and the pad. This interaction causes an increase in energy dissipation into the template, which leads to high-frequency vibrations that likely cause damage to the secondary steel. The template is also exposed to more blows while installing one foundation pile. However, it couldn't be proven that the current design is the only cause of damage to the secondary steel of the pre-piling template. More extensive research and validation should be done to prove the hypothesis fully.

6.2. Recommendations

6.2.1. Recommendations for further research

For future research, it is recommended that the pile is not modeled as a rigid body but incorporate flexibility to allow for wave propagation and radial expansion due to pile driving. A combination of the interaction of the friction pads, wave propagation and radial expansion of the pile due to the impact force of the hammer could show an increase or decrease of energy dissipation into the pre-piling template. Another recommendation is to incorporate the template geometry as well as its secondary steel. Then a study can be done into the vibrations of the secondary steel and template to say something about the vibrations and energy dissipation into the secondary steel.

Also, the effect of hydrodynamic loads on the installation process should be taken into account in future research. Hydrodynamic loads can cause the foundation piles to sway or bend, leading to an asymmetrical load on the pads. This could cause asymmetrical distribution of loads and lead to possible changes to the energy flow between the pile and the template.

6.2.2. Recommendations for Huisman

For future design choices of pre-piling templates, it would be recommended to reconsider using rollers. Since rollers have a smaller friction coefficient than friction pads, the dissipation of energy into the pre-piling template due to friction forces could be less. Another design of the upper centralizer also could be considered. Change the design of the centralizer so that the rotation point is above the pads. In this orientation, there probably will not be a self-reinforcing effect on the normal force during pile driving.

The field data gathered by Huisman during the use of the pre-piling template was measured at 1Hz and only with one accelerometer in the middle of the pad. However, to validate the results from chapter 5, it is recommended to install accelerometers on the pads and sleeves. The frequency of the sensors should be in the range of the impact of the hammer. In chapter 4, it can be seen that the typical duration of the impact of a hammer is around 0.015 seconds. To measure the influence of the impact accurately, it is recommended to increase the frequency of the sensors. Zampolli [42] experimented to validate the predictions of underwater noise. To measure the accelerations and vibrations in the pile induced by the hammer impact, an accelerometer with a sampling rate of 5 kHz was used. The impact characteristics of the hammer used are the same as those used in this research. To prevent big data sets, the measurements need to be timed tactically.

Bibliography

1. B.V., H. E. *about Huisman* https://www.huismanequipment.com/en/about_huisman. (accessed: 01.05.2023).
2. Agency, I. E. *World Energy Outlook 2022* https://www.iea.org/reports/world-energy-outlook-2022. (accessed: 02.05.2023).
3. Administration, U. E. I. *International Energy Outlook 2020* https://www.eia.gov/outlooks/ieo/. (accessed: 02.05.2023).
4. Nations, U. *Adoption of the Paris Agreement* https://unfccc.int/sites/default/files/english_paris_agreement.pdf. (accessed: 02.05.2023).
5. Agency, T. I. R. E. *Renewable Energy Statistics 2022* https://www.irena.org/Publications/2022/Jul/Renewable-Energy-Statistics-2022. (accessed: 03.05.2023).
6. Olsen, F. & Dyre, K. Vindeby Off-Shore Wind Farm-Construction and Operation Vindeby Off-Shore Wind Farm-Construction and Operation Paper presented at a BWEA/DTI/Multi-Science Seminar on Prospects for Offshore Wind. *Source: Wind Engineering* **17,** 120–128 (1993).
7. WindEurope. *History of Europe's wind industry* https://windeurope.org/about-wind/history/. (accessed: 03.05.2023).
8. Wang, L., Kolios, A., Liu, X., Venetsanos, D. & Rui, C. Reliability of offshore wind turbine support structures: A state-of-the-art review. *Renewable and Sustainable Energy Reviews* **161,** 112250. ISSN: 1364-0321 (June 2022).
9. Van der Male, P. *OE44135 2019 Lecture Notes 1 - Design Procedure* 2013.
10. Offshore wind in Europe - key trends and statistics 2020 (2021).
11. *Changfang and Xidao - Copenhagen Infrastructure Service Company* https://cisc.dk/assets/changfang-and-xidao/.
12. *navantia_20180306.jpg (662×538)* https://w3.windfair.net/uploads/notice/preview/27611/navantia_20180306.jpg.
13. Klijnstra, J., Zhang, X., van der Putten, S. & Röckmann, C. Technical risks of offshore structures. *Aquaculture Perspective of Multi-Use Sites in the Open Ocean: The Untapped Potential for Marine Resources in the Anthropocene,* 115–127 (Apr. 2017).
14. Hoving, J. *OE44096 Bottom Founded Offshore Structures - Substructure design: Geometry and Configuration* 2019.
15. Huisman. *Internal Huisman Server* 2023.
16. Ruijgrok, R. *Design optimization of an adjustable Pre-Piling-Template: for wind-turbine installation* 2019. https://repository.tudelft.nl/islandora/object/uuid%3A2d7ae85a-aa2a-462b-8a03-09332febe689.
17. Bosma, M. *Optimization of the installation sequence of an Offshore Wind Farm Monopile Installation Template: by improving the foundation design* 2023. https://repository.tudelft.nl/islandora/object/uuid%3A339e55ba-2f8f-4c7c-b74d-0d30a98781ea.
18. Van Gils, M. *Swaying piles during installation with seabed templates: Modelling dynamic behavior and a solution* 2020. https://repository.tudelft.nl/islandora/object/uuid%3A41299469-4f95-4bdd-9db0-247f159c3d87.
19. Zwartveld, J. *Structural vibrations induced by pile driving* 2016. https://repository.tudelft.nl/islandora/object/uuid%3A782ecc4b-3d55-40ab-bb14-120a115921f3.

20. Rietema, B. *Uplift behavior of offshore shallow foundations during retrieval: An experimental study on the pressure differences that occur during uplift of mud-mats of pre-piling templates* 2022. https://repository.tudelft.nl/islandora/object/uuid%3Ac911b76e-6774-4afb-9674-e229d19236c6.

21. Pitenis, A. A., Dowson, D. & Gregory Sawyer, W. Leonardo da Vinci's friction experiments: An old story acknowledged and repeated. *Tribology Letters* **56,** 509–515. ISSN: 15732711. https://link.springer.com/article/10.1007/s11249-014-0428-7 (Nov. 2014).

22. *Théorie des machines simples en ayant égard au frottement de leurs parties ... - Charles Augustin Coulomb - Google Boeken* https://books.google.nl/books?hl=nl&lr=&id=7lRJAAAAcAAJ&oi=fnd&pg=PA4&ots=GWMH2bMDXs&sig=Swkr_VKH0ym25wcLblTJUZXA-Qg&redir_esc=y#v=onepage&q&f=false.

23. Dupont, P., Hayward, V., Armstrong, B. & Altpeter, F. Single state elastoplastic friction models. *IEEE Transactions on Automatic Control* **47,** 787–792. ISSN: 00189286 (May 2002).

24. Marques, F., Woliński, Ł., Wojtyra, M., Flores, P. & Lankarani, H. M. An investigation of a novel LuGre-based friction force model. *Mechanism and Machine Theory* **166.** ISSN: 0094114X (Dec. 2021).

25. Gagnon, L., Morandini, M. & Ghiringhelli, G. L. A review of friction damping modeling and testing. *Archive of Applied Mechanics* **90,** 107–126. ISSN: 14320681. https://link.springer.com/article/10.1007/s00419-019-01600-6 (Jan. 2020).

26. Marques, F., Flores, P., Claro, J. C. & Lankarani, H. M. Modeling and analysis of friction including rolling effects in multibody dynamics: a review. *Multibody System Dynamics* **45,** 223–244. ISSN: 1573272X (Feb. 2019).

27. Leine, R. I., Van Campen, D. H., De Kraker, A. & Van Den Steen, L. Stick-Slip Vibrations Induced by Alternate Friction Models. *Nonlinear Dynamics* **16,** 41–54. ISSN: 0924090X. https://link.springer.com/article/10.1023/A:1008289604683 (1998).

28. Dahl, P. R. Solid Friction Damping of Mechanical Vibrations. *https://doi.org/10.2514/3.61511* **14,** 1675–1682. ISSN: 00011452. https://arc.aiaa.org/doi/10.2514/3.61511 (May 2012).

29. Wit, C. C. d., Olsson, H., Åström, K. J. & Lischinsky, P. A New Model for Control of Systems with Friction. *IEEE Transactions on Automatic Control* **40.** ISSN: 0018-9286. https://portal.research.lu.se/en/publications/a-new-model-for-control-of-systems-with-friction (1995).

30. *Publication – Comparison of Two Versions of the LuGre Model Under Conditions of Varying Normal Force – Warsaw University of Technology* https://repo.pw.edu.pl/info/article/WUT2eb80cb178fa4d4f836f612324d0e43c/.

31. Smith, E. Pile-Driving Analysis by the Wave Equation. *Transactions of the American Society of Civil Engineers* **127,** 1145–1171. ISSN: 0066-0604. https://ascelibrary.org/doi/abs/10.1061/TACEAT.0008471%20https://ascelibrary.org/doi/10.1061/TACEAT.0008471 (Jan. 1962).

32. *(PDF) Application of characteristic stress wave method in offshore practice* https://www.researchgate.net/publication/280235382_Application_of_characteristic_stress_wave_method_in_offshore_practice.

33. Deeks, A. J. & Randolph, M. F. Analytical modelling of hammer impact for pile driving. *International Journal for Numerical and Analytical Methods in Geomechanics* **17,** 279–302. ISSN: 10969853 (1993).

34. *Choose an ODE Solver - MATLAB & Simulink - MathWorks Benelux* https://nl.mathworks.com/help/matlab/math/choose-an-ode-solver.html.

35. Jiang, Q. *et al.* Theoretical study of vibro-acoustics of fluid-pile-soil coupled system and experimental research of noise reduction of small-scale pile driving. *Ocean Engineering* **252,** 110997. ISSN: 0029-8018 (May 2022).

36. Rill, G., Schaeffer, T. & Schuderer, M. LuGre or not LuGre. *Multibody System Dynamics.* ISSN: 1384-5640. https://link.springer.com/10.1007/s11044-023-09909-5 (May 2023).

37. Steel Sheet Pile Guides • Basic Principles of Hammers for Sheet Pile Installation PILE DRIVING CONTRACTORS ASSOCIATION STEEL SHEET PILE GUIDES BASIC PRINCIPLES OF HAMMERS FOR SHEET PILE INSTALLATION. www.piledrivers.org.

38. Jacobson, B. The Stribeck memorial lecture. *Tribology International* **36,** 781–789. ISSN: 0301-679X (Nov. 2003).

39. Fuhg, J. N., Fau, A., Fuhg, J. N. & Fau, A. Surrogate model approach for investigating the stability of a friction-induced oscillator of Duffing's type. **98,** 1709–1729. https://doi.org/10.1007/s11071-019-05281-2 (2019).

40. Boskalis. *Soil data provided by Boskalis* 2021.

41. Chen, S. & Zhang, Z. Modification of friction for straightforward implementation of friction law. *Multibody System Dynamics* **48,** 239–257. ISSN: 1573272X (Feb. 2020).

42. Zampolli, M. *et al.* Validation of finite element computations for the quantitative prediction of underwater noise from impact pile driving. *The Journal of the Acoustical Society of America* **133,** 72–81. ISSN: 0001-4966. eprint: https://pubs.aip.org/asa/jasa/article-pdf/133/1/72/14805798/72_1_online.pdf. https://doi.org/10.1121/1.4768886 (Jan. 2013).

A

Derivations

All the derivations used in Subsection 3.2.3 are presented in this appendix. The small angle approximation is used for θ in all the derivations. The small angle approximation can be used when θ « 0. The following approximations can be made for all the derivations where theta is used (Equation A.1).

$$\sin\theta \approx \theta, \quad \cos\theta \approx 1 - \frac{\theta^2}{2} \approx 1, \quad \tan\theta \approx \theta \tag{A.1}$$

A.1. Derivations

A.1.1. Derivation of M_h and M_v

In Figure A.1, a closeup of point A can be seen. This section clarifies the derivation of the contributing forces F_h and F_v. First, the moments around point c are described. The forces used for the moment are chosen perpendicular to the arm L_β, so M_h and M_v can be written as Equation A.2. Then the forces F_v and F_h written in the normal plane of the system can be expressed by F_v' and F_h' (Equation A.3) substitute in Equation A.2 will result in Equation A.5.

$$\begin{aligned} M_h &= F_h' L_\beta \\ M_v &= F_v' L_\beta \end{aligned} \tag{A.2}$$

$$\begin{aligned} sin(\beta) &= \frac{F_h'}{F_h} \\ cos(\beta) &= \frac{F_v'}{F_v} \end{aligned} \tag{A.3}$$

$$\begin{aligned} F_h' &= F_h sin(\beta) \\ F_v' &= F_v cos(\beta) \end{aligned} \tag{A.4}$$

$$\begin{aligned} M_h &= F_h L_\beta sin(\beta) \\ M_v &= F_v L_\beta cos(\beta) \end{aligned} \tag{A.5}$$

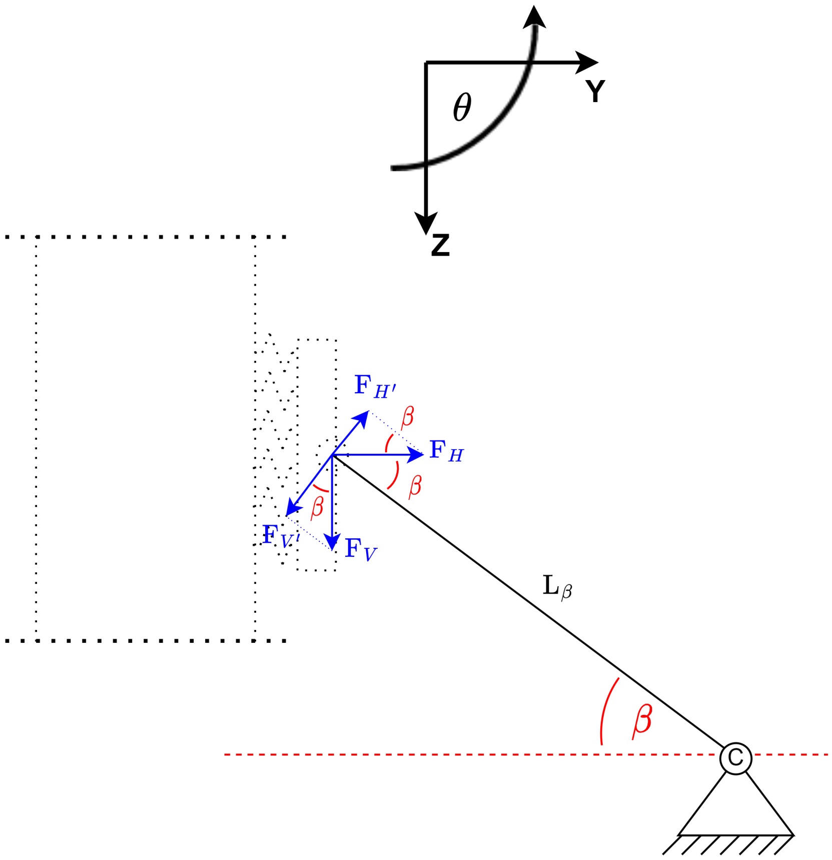

Figure A.1: Close up of point A to derive Mh and Mv

A.1.2. Derivation of M_{cyl}

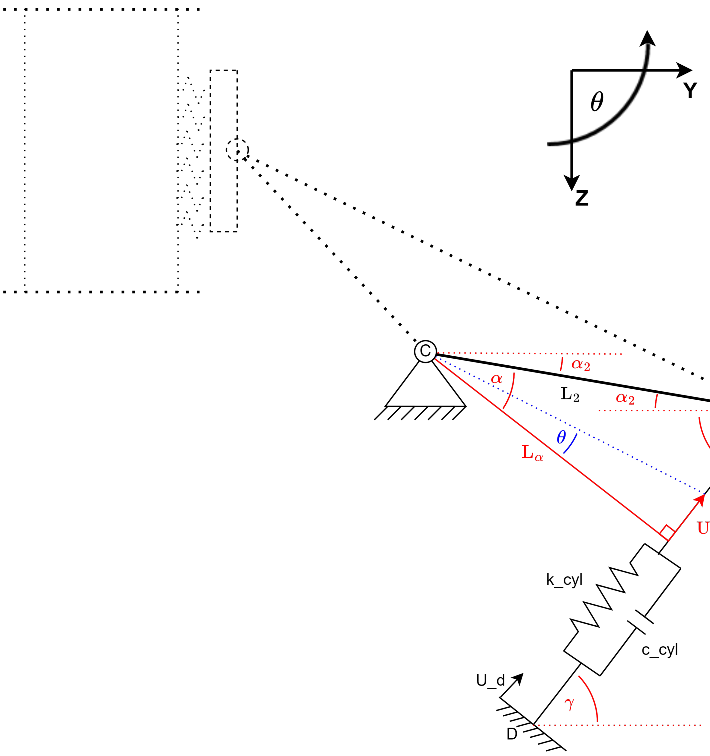

Figure A.2: Close up of point B to derive Mcyl

The force applied by the cylinder and damper is determined by the displacement of points B and D and The velocity of point B. In Equation A.6, the derivation of the displacement and velocity of point B is shown. With the approach of the arm L_α (Equation A.7) chosen perpendicular to B-D, there is no need to use the horizontal and vertical displacement and velocity of B and the use of arm L2. U_d will be calculated in Appendix A.1.4. The positive direction of the force is applied due to a positive U_d displacement. The displacement of B will lead to a decrease in the force the cylinder applies.

$$\begin{aligned} U_b &= L_\alpha tan(\theta) \approx L_\alpha \theta \\ \dot{U}_b &= L_\alpha \dot{\theta} \end{aligned} \tag{A.6}$$

$$L_\alpha = L_2 \cos(\alpha) \tag{A.7}$$

From Equation A.6, the stiffness and damping of the cylinder (k_{cyl} and c_{cyl}) the cylinder force can be calculated using Equation A.8. Ultimately the moment due to the cylinder can be described as Equation A.9 due to the perpendicular chosen arm L_α.

$$F_{cyl} = k_{cyl}(U_d - U_b) + c_{cyl}(\dot{U}_d - \dot{U}_b) \tag{A.8}$$

$$\begin{aligned} M_{cyl} &= F_{cyl} L_\alpha \\ &= k_{cyl}(U_d - L_\alpha \theta) L_\alpha + c_{cyl}(\dot{U}_d - L_\alpha \dot{\theta}) \end{aligned} \tag{A.9}$$

A.1.3. Derivation of F_h

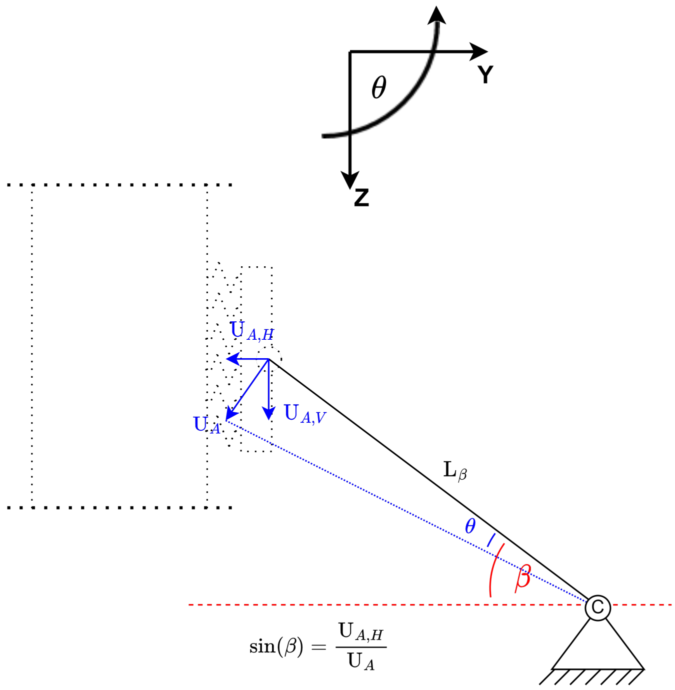

Figure A.3: Close up of point A to derive Fh

The rotation of the triangle describes F_h, and consequently, the horizontal motion of A described as $U_{A,H}$. $U_{A,H}$ follows from U_A which is calculated in Equation A.10. Due to the equivalent stiffness k_{eq} of the pile and the horizontal displacement of A, the force F_h can be derived. From Subsection A.1.3, the following equations can be determined.

$$U_A = L_\beta tan(\theta) \approx L_\beta \theta \tag{A.10}$$

$$\begin{aligned} F_h &= k_{eq} U_{A,H} \\ &= k_{eq} U_A sin(\beta) \\ &= k_{eq} L_\beta \theta sin(\beta) \end{aligned} \tag{A.11}$$

A.1.4. Calculation of U_d

to be applied by the pad. In point A, the pretension is applied as a force F_{pre}. To calculate the initial rotation of the upper centralizer, Equation A.12 and Equation A.13 are used.

$$\begin{aligned} F_{pre} &= F_{h,init} \\ &= k_{eq} L_\beta \theta_{init} sin(\beta) \end{aligned} \tag{A.12}$$

$$\theta_{init} = \frac{F_{pre}}{k_{eq} L_\beta sin(\beta)} \tag{A.13}$$

To prevent the hydraulic cylinder (k_{cyl} and c_{cyl}) from applying a counter moment on the upper centralizer, the initial length of the hydraulic cylinder needs to be corrected. This can be done by moving point D. U_D can be calculated using L_α and θ_{init} see Equation A.14.

$$U_D = L_\alpha \theta_{init} \tag{A.14}$$

B

Equivalent radial stiffness of the pile

To calculate the equivalent stiffness of the pile, ANSYS is used to perform a Finite Element Analysis to calculate the equivalent stiffness of the pile. First, a 3D model was made with the software Rhino6. The pile parameters used can be seen in Table B.1, assuming the pile is made of structural steel. The length of the pile is taken so that it does not influence the results of the FEA. However, not the entire length of the pile is modeled.

D_{pile} [m]	t_{pile} [m]
3.5	0.05

Table B.1: Foundation pile parameters

In Figure B.1, the mesh made for the FEA can be seen. The places where the pads will apply a force are meshed finer to obtain more accurate results at those places since they are the places of interest. A force is applied in the normal direction at all four places. The pads should have exerted a force. A symmetrical approach is chosen because the pile-template interaction model also assumes symmetrical loads.

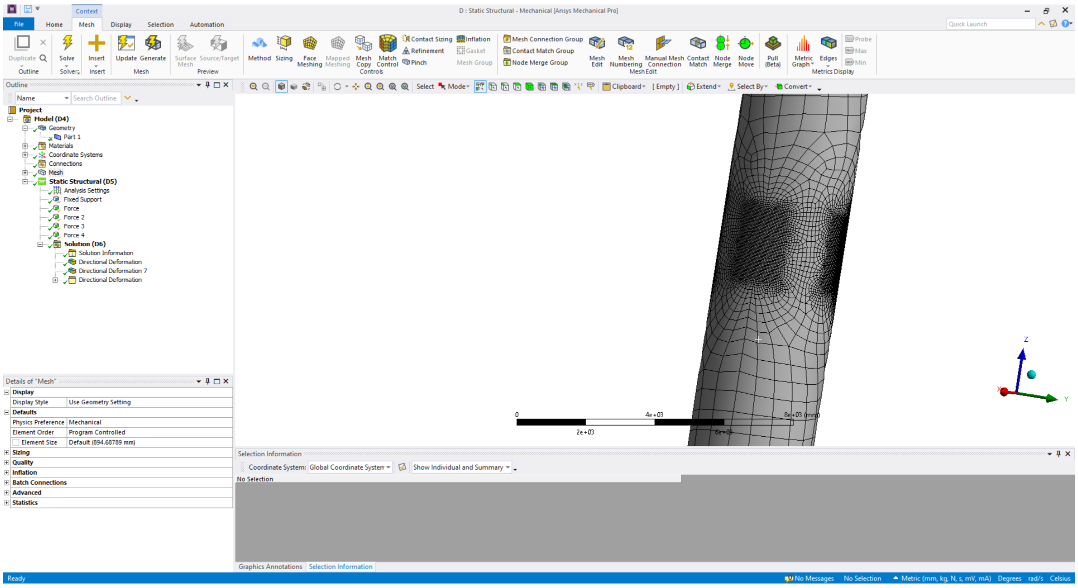

Details of "Mesh"

Display	
Display Style	Use Geometry Setting
Defaults	
Physics Preference	Mechanical
Element Order	Program Controlled
☐ Element Size	Default (894.68789 mm)
Sizing	
Quality	
Inflation	
Batch Connections	
Advanced	
Statistics	

Figure B.1: Picture of the mesh made in ANSYS

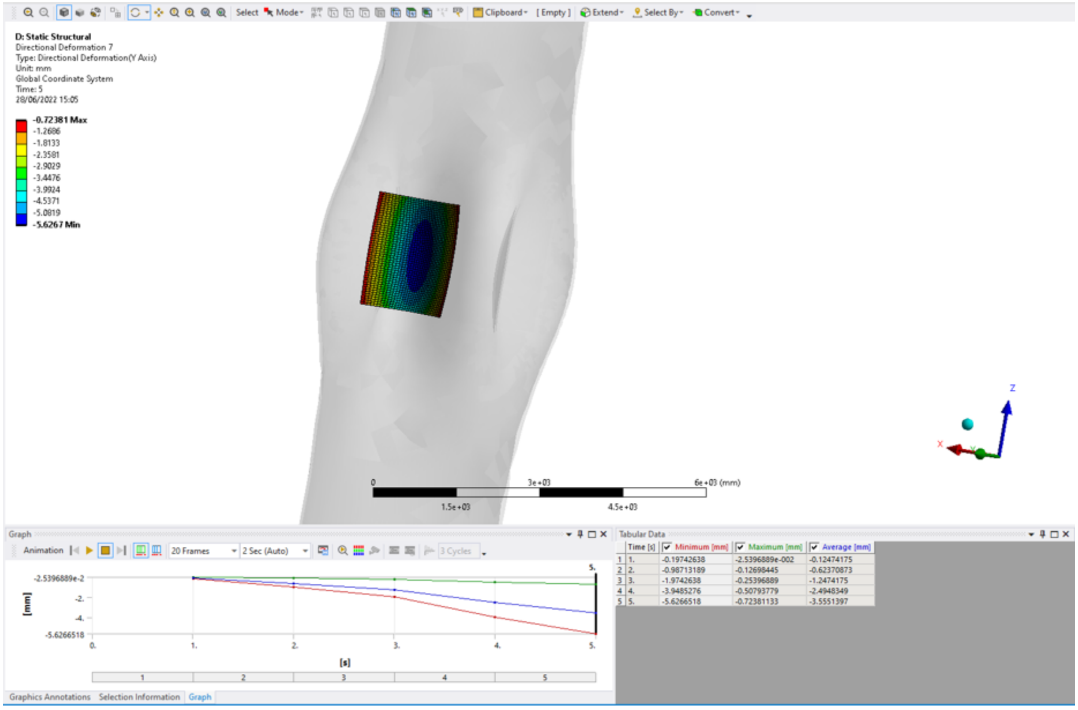

D: Static Structural
Directional Deformation 7
Type: Directional Deformation(Y Axis)
Unit: mm
Global Coordinate System
Time: 5
28/06/2022 15:05

	Time [s]	☑ Minimum [mm]	☑ Maximum [mm]	☑ Average [mm]
1	1.	-0.19742638	-2.5396889e-002	-0.12474175
2	2.	-0.98713189	-0.12698445	-0.62370873
3	3.	-1.9742638	-0.25396889	-1.2474175
4	4.	-3.9485276	-0.50793779	-2.4948349
5	5.	-5.6266518	-0.72381133	-3.5551397

Figure B.2: The results of the ANSYS FEA of the pile.

In Figure B.2, the results of the FEA can be seen. The deformations are enlarged to be able to see the deformation. The choice is made to use the average deformation of the area of the pads. Using Equation B.1, the stiffness of the pile can be calculated. In Table B.2, the results of the FEA are presented. The equivalent stiffness of the pile is k_{eq} = 497 $[kN/m]$.

$$k_{eq} = \frac{F}{u} \tag{B.1}$$

F[kN]	F [N]	u [mm]	k_{eq} [N/m]
10	98100	0.197426	496894.1
50	490500	0.987132	496894.1
100	981000	1.974264	496894.1
200	1962000	3.948528	496894.1
285	2795850	5.626652	496894.1

Table B.2: Results of the FEA

C

Inertia triangle

In this Appendix, the mass moment of inertia around point C is derived using the rectangular triangle technique. The object, in this case, the upper centralizer, is divided into rectangular triangles. This can be seen in Figure C.1. The centralizer is split into three big triangles, the blue 1, 2, and 3, and two small triangles, the green 4 and 5. To calculate the total mass moment of inertia, the inertia of the green triangles will be subtracted from the blue triangles. In Equation C.4 to Equation C.8, the mass moment of inertia is calculated, where dm $[kg/m^2]$ is the distributed mass of the upper centralizer. Using the derivations in Appendix A, y_1, y_2, y_{-1}, z_1, z_2 and z_{-1} are derived using Equation C.1 and Equation C.2. After calculating the mass moment of inertia per triangle, the total mass moment of inertia is calculated using Equation C.3.

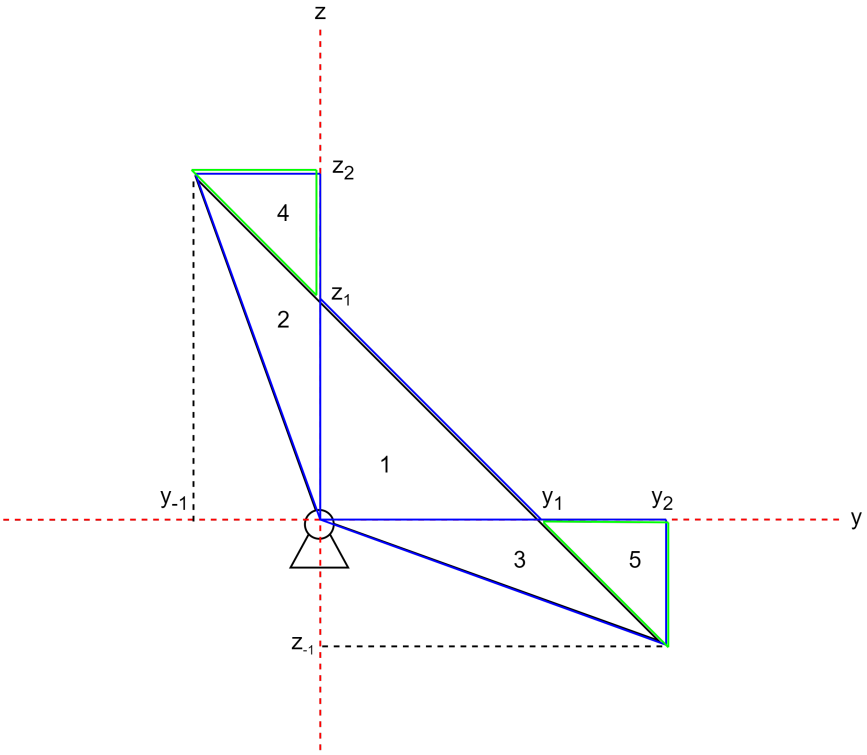

Figure C.1: The upper centralizer is split up in right-angled triangles to calculate the mass moment of inertia

$$\begin{aligned} y_2 &= y_B = L_2 \cos(\alpha_2) \\ y_{-1} &= y_A = -L_\beta \cos(\beta) \\ z_2 &= z_A = L_\beta \sin(\beta) \\ z_{-1} &= z_B = -L_2 \sin(\alpha_2) \end{aligned} \tag{C.1}$$

$$\begin{aligned} y_1 &= y_2 - \frac{y_2 - y_{-1}}{z_2 - z_{-1}}(z - z_{-1}) \text{ where, } z = 0 \\ z_1 &= z_2 - \frac{z_2 - z_{-1}}{y_2 - y_{-1}}(y - y_{-1}) \text{ where, } y = 0 \end{aligned} \tag{C.2}$$

$$I_{triangle} = I_1 + I_2 + I_3 - I_4 - I_5 \tag{C.3}$$

$$I_1 = (1/3)y_1 z_1 (y_1^2 + z_1^2)dm \tag{C.4}$$

$$I_2 = (1/3)y_{-1} z_2 (y_{-1}^2 + z_2^2)dm \tag{C.5}$$

$$I_3 = (1/3)y_2 z_{-1} (y_2^2 + z_{-1}^2)dm \tag{C.6}$$

$$\begin{aligned} I_4 = {} & ((1/3)y_{-1}(y_{-1}^2 + z1^2)(z_1 - z_2) \\ & + (1/2)(z_2 - z_1)abs(y_{-1})(((2/3)(z_2 - z_1) + z_1)^2 + ((1/3)y_{-1})^2))dm \end{aligned} \tag{C.7}$$

$$\begin{aligned} I_5 = {} & ((-1/3)z_{-1}(y_1 - y_2)(y_1^2 + y_1 y_2 + y_2^2 + z_1^2) \\ & + (1/2)(y_2 - y_1)abs(z_{-1})(((1/3)z_{-1})^2 + (y_1 + (2/3)(y_2 - y_1))^2))dm \end{aligned} \tag{C.8}$$

D

Derivation of doubled hammer energy

In this Appendix, the derivations are shown to determine the ratio of the impact velocity v_0 and the hammer force $F(t)$ when the amount of energy inputted by the hammer is doubled. The hammer force is described by Equation D.1, where $F(t)$ is the hammer force over time, Z is the pile impedance and $\bar{F}(t)$ is the dimensionless hammer force. This equation is also described in Subsection 3.2.1. The impact speed v_0 is described by Equation D.2. In this equation, E_{hammer} is the input energy of the hammer, and m_{ram} is the mass of the ram.

$$F(t) = Zv_0\bar{F}(t) \tag{D.1}$$

$$v_0 = \sqrt{\frac{2E_{hammer}}{m_{ram}}} \tag{D.2}$$

To compare the ratio between the velocities of the hammer when the energy is normal and doubled v_{0_1} and v_{0_2} are introduced. v_{0_1} is the impact speed when the hammer energy is taken once, and v_{0_2} is when the hammer energy is doubled. The derivation of both velocities can be seen in Equation D.3 and Equation D.4.

$$\begin{aligned} v_{0_1} &= \sqrt{\frac{2E_{hammer}}{m_{ram}}} \\ &= \sqrt{2}\sqrt{\frac{E_{hammer}}{m_{ram}}} \end{aligned} \tag{D.3}$$

$$\begin{aligned} v_{0_2} &= \sqrt{\frac{2 \cdot 2E_{hammer}}{m_{ram}}} \\ &= 2\sqrt{\frac{E_{hammer}}{m_{ram}}} \end{aligned} \tag{D.4}$$

The ratio between the two velocities can be seen in Equation D.5 and Equation D.6. It was shown that by doubling the amount of energy the impact velocity increases by $\sqrt{2}$.

$$\frac{v_{0_2}}{v_{0_1}} = \frac{2\sqrt{\frac{E_{hammer}}{m_{ram}}}}{\sqrt{2}\sqrt{\frac{E_{hammer}}{m_{ram}}}} \tag{D.5}$$

$$v_{0_2} = \sqrt{2}v_{0_1} \tag{D.6}$$

To calculate the increase in hammer force, $F_1(t)$ and $F_2(t)$ are introduced, where $F_1(t)$ is the hammer force when the input energy is taken once and $F_2(t)$ is the hammer force when the input energy is doubled. See Equation D.7 and Equation D.8. The pile impedance and the dimensionless force remain the same.

$$F_1(t) = Zv_{0_1}\bar{F}(t) \tag{D.7}$$

$$F_2(t) = Zv_{0_2}\bar{F}(t) \tag{D.8}$$

Substituting Equation D.6 into Equation D.8 gives Equation D.9. Deriving the ratio between the forces by dividing $F_2(t)$ by $F_1(t)$ gives us Equation D.10 and ultimately Equation D.11. Where it can be seen that the force increases by $\sqrt{2}$ when doubling the input energy of the hammer.

$$F_2(t) = Z\sqrt{2}v_{0_1}\bar{F}(t) \tag{D.9}$$

$$\frac{F_2(t)}{F_1(t)} = \frac{Z\sqrt{2}v_{0_1}\bar{F}(t)}{Zv_{0_1}\bar{F}(t)} = \sqrt{2} \tag{D.10}$$

$$F_2(t) = \sqrt{2}F_1(t) \tag{D.11}$$